Geochemistry, Geophysics, Geosystems

RESEARCH ARTICLE
10.1002/2017GC007266

The Sensitivity of Core Heat Flux to the Modeling of Plate-Like Surface Motion

Sean M. Langemeyer[1], Julian P. Lowman[1,2], and Paul J. Tackley[3]

[1]Department of Physics, University of Toronto, Toronto, ON, Canada, [2]Department of Physical and Environmental Sciences, University of Toronto Scarborough, Toronto, ON, Canada, [3]Department of Earth Sciences, ETH Zurich Institute Fuer Geophysik, Zurich, Switzerland

Key Points:
- Self-consistently modeled plates and current-day core heat loss can be simultaneously obtained
- Internal heating can be used to mitigate core heat loss for plate-like surface regime systems
- Modeling intrinsically dense provinces does not adversely affect modeling plates

Supporting Information:
- Table S1

Correspondence to:
S. M. Langemeyer,
sean.langemeyer@mail.utoronto.ca

Citation:
Langemeyer, S. M., Lowman, J. P., & Tackley, P. J. (2018). The sensitivity of core heat flux to the modeling of plate-like surface motion. *Geochemistry, Geophysics, Geosystems*, *19*, 1282–1308. https://doi.org/10.1002/2017GC007266

Received 29 SEP 2017
Accepted 6 MAR 2018
Accepted article online 6 APR 2018
Published online 20 APR 2018

Abstract The generation of a magnetic field and the presence of tectonic plates are fundamental aspects of Earth's evolution. Viable dynamic models of terrestrial mantle convection therefore require the existence of heat transport from the core and a surface characterized by piecewise uniform surface velocity domains (i.e., plates). To test the compatibility of these two requirements, we varied energy input, rheology, and compositional heterogeneity in more than 70 mantle convection simulations. Calculations are performed in a spherical annulus geometry. By systematic investigation, we demonstrate that Earth-like core heat flux can be obtained with self-consistent model plates. We find that, given an initial condition where model parameters are chosen to ensure a mobile surface, the mobility is not strongly influenced when H is varied by up to a factor of three. Consequently, in spherical models with steady core temperatures and internal heating rates, the latter quantity can be used to regulate core heat flow to fit within the bounds inferred for terrestrial values. In contrast, core heat flow is strongly sensitive to model yield stress. We systematically vary thermal viscosity contrast, an intrinsic depth-dependent viscosity and the depth-dependence of a stress-dependent rheology and analyze how each factor affects both surface velocities and core heat flux. Finally, we show that the addition of an intrinsically dense component comprising 5% or less of the mantle volume does not affect surface mobility or plateness, although it can have a profound impact on heat loss from the core.

1. Introduction

The existence of plate-like surface motion and the generation of a magnetic field are possibly the most rudimentary requirements that any global geodynamic model of the present-day Earth must feature. Working within the limitations of mantle convection modeling, the latter physical requirement imposes constraints on core-mantle boundary (CMB) heat flux. By influencing surface heat flux and focusing the flux of cold material, plate tectonics principally controls the temperature of the mantle by the process of subduction (e.g., Coltice et al., 2017; Combes et al., 2012; Monnereau & Quéré, 2001). Globally, the rate of subduction, spatial distribution of subduction zones, and longevity of subduction (once initiated) act together to influence mantle temperatures (Bercovici et al., 1989). The thermal gradient across the CMB is determined by the ambient temperature of the mantle relative to the outer core (Buffett, 2003, 2007; Lay et al., 2008). Consequently, the existence of plate tectonics influences the rate of core heat loss and the ability of Earth to generate a magnetic field. However, heat flux from the core allows for the generation of plumes (Labrosse, 2002), which may affect surface motion by producing stress in the lithosphere (Korenaga, 2017; Ratcliff et al., 1998; Weller & Lenardic, 2016; Zhong & Watts, 2002) while also influencing upper mantle rheology. Given this coupling, between surface mechanics and core heat loss, an investigation of the necessary ingredients for plate tectonics must be constrained by the requirement of obtaining a CMB heat flux consistent with the energy requirements of the geodynamo.

Bounds have been placed on core heat flux through several lines of argument. Estimating the heat flux associated with hot spots, and then assuming that the origin of hot spots derives from plumes that carry all of their heat to the base of the lithosphere, provides one method of determining the heat flow across the CMB (Buffett, 2007; Labrosse, 2002; Sleep, 1990). Such analyses provide a lower bound on core heat loss of 2–2.5 TW (Bunge, 2005; Davies, 1988; Labrosse, 2002; Mittelstaedt & Tackley, 2006). Larger estimates are determined through simulations of the geodynamo (Kuang & Bloxham, 1997; Labrosse et al., 1997). For

example, estimates of ohmic heat dissipation and secular cooling provide constraints on the thermal history of the core rooted in calculations of the energy flow required by magnetic field observations (Buffett, 2002; Christensen & Tilgner, 2004; Labrosse, 2003). Independently, even greater estimates of the heat loss from the core are determined from the inferred conductivity of iron at the extreme pressures and temperatures found at the core-mantle boundary (Labrosse, 2015; Pozzo et al., 2012) with calculated estimates suggesting an adiabatic heat flow of nearly 15 TW.

Collectively, studies constraining heat loss from the core yield a range from 2 to 15 TW (Buffett, 2003; Gubbins et al., 2015; Labrosse, 2015; Lay et al., 2006; Pozzo et al., 2012). Given the estimated total heat flow of the Earth of 47 $\pm$ 2 TW (Davies & Davies, 2010; Jaupart et al., 2007; Lay et al., 2008; Turcotte & Schubert, 2014) and the 3–8 TW estimate of heat coming from the crust (Pollack & Chapman, 1977a, 1977b; Rudnick & Fountain, 1995;-Stacey & Davis, 2008) models of the core's evolution suggest that its heat loss accounts for 5–40% of the heat coming from the mantle. Due to the relatively small area of the CMB compared with the Earth's surface even a contribution of 5% of the surface heat flow from the core results in the formation of a thermal boundary layer adjacent to the CMB. Accordingly, mantle convection models of the present-day Earth, featuring self-consistently generated plate tectonics, should include a strong thermal gradient in the deep mantle either enveloping the core or lying over the core and any deep compositional anomalies.

The generation of a stiff lithosphere results from an exponentially varying temperature-dependent rheology. However, none of the resulting convective regimes generated through a purely temperature-dependent viscosity yield a surface that can be considered plate-like (i.e., featuring a surface possessing narrow regions of high deformation with high velocity gradients bounding regions of minimal deformation and a near zero lateral velocity gradient) (Christensen, 1984; Solomatov, 1995). Augmentation of a temperature-dependent rheology with a stress-dependence (Loddoch et al., 2006; Moresi & Solomatov, 1998; Stein et al., 2004; Tackley, 2000a, 2000b; Trompert & Hansen, 1998) allows for foundering of the upper thermal boundary layer and the first-order modeling of processes analogous to subduction and divergence at plate boundaries (Bercovici, 2003). A primary ramification of enabling surface mobility is a profound impact on mantle temperature and core heat flux (Stein & Lowman, 2010).

The dependence of mantle viscosity on depth has been investigated through a multitude of studies including investigations of postglacial rebound (Mitrovica & Forte, 2004; Mitrovica & Peltier, 1991; Sigmundsson, 1991; Turcotte & Schubert, 2014) and the response of the geoid to viscosity gradients (Hager, 1984). These studies infer a viscosity of 10^{21} Pa s averaged over the top 1,000 km (Haskell, 1935; Lambeck et al., 1996, 1998; Mitrovica, 1996; Mitrovica & Forte, 1997) and a viscosity increase of a factor of 30 or greater at a depth approximately coinciding with the 660 km phase transition (Hager, 1984; King & Masters, 1992; Mitrovica & Forte, 2004; Richards & Hager, 1984). (More recent work has inferred a significant jump in viscosity commencing at depths between 800 and 1,200 km but has not identified an initiating mechanism for the increase, Marquardt & Miyagi, 2015; Rudolph et al., 2015.) Accordingly, relevant mantle convection models featuring plate tectonics should include a viscosity that increases sharply with depth at the bottom of the upper mantle but also penetration of the lower mantle by downwellings in at least some locations. Decreases in asthenospheric viscosity (Höink & Lenardic, 2008, 2010; Richards et al., 2001; Stein et al., 2004, 2011; Tackley, 2000a, 2000b) and increases in lower mantle viscosity relative to the viscosity of the upper mantle enhance plate-like features. Individually, reductions in lower mantle/upper mantle viscosity contrast and increases in thermal viscosity contrast each act to reduce surface mobility (Gait et al., 2008; Stein & Hansen, 2008).

Due to computational constraints many studies focusing on the generation of plate tectonics have been presented in Cartesian geometries, with a relative few analyzed in 3-D spherical geometries (Foley & Becker, 2009; Mallard et al., 2016; van Heck & Tackley, 2008). Calculations employing spherical geometries involving low to moderate Rayleigh numbers (in comparison to a terrestrial value), low yield stress, and a temperature-dependent viscosity, showed that self-consistent plate-like surface motion could be generated in global models and found results featuring dominantly degree 1 and 2 convection (Foley & Becker, 2009; van Heck & Tackley, 2008; Yoshida, 2008).

In this study, we focus on the feasibility of obtaining a plate-like surface velocity field while constraining interior mantle properties to match characteristics such as an intrinsic increase in viscosity in the lower mantle (below a depth of 660 km) and a core derived energy input to mantle convection compatible with

estimates of current-day contributions to the surface heat flux. We employ a temperature-dependent rheology with pseudoplastic yielding as a starting point for achieving surface mobility while modeling a stiff lithosphere, and an isothermal core-mantle boundary in order to obtain core heat flow. Previous studies have shown the critical influences of yield stress and internal heating on obtaining mobile but plate-like surface motion (where the latter notion is defined by a surface characterized by broad regions exhibiting minimal strain rates separated by narrow regions featuring high velocity gradients; that is, plate boundaries). Starting with yield stress and the nondimensional internal heating rate, we identify parameter values that allow for a ratio of core to surface heat flux within the range supported by current studies. Subsequently, we investigate refining the surface characteristics to obtain increasingly plate-like surface features while maintaining the desired percentage of core heat flux. Finally, we investigate how the introduction of a dense component in the mantle, owing to compositional difference, has a bearing on plates and core heat flow.

2. Methods

2.1. Governing Equations

Mantle convection is modeled in a spherical annulus geometry using the finite volume code STAGYY (Tackley, 2000a). We solve the dimensionless equations for mass, momentum, and energy conservation in a bimodally heated infinite Prandtl number Boussinesq fluid; specifically:

$$\nabla \cdot \mathbf{u}=0, \tag{1}$$

$$\nabla \cdot [\eta(\nabla \mathbf{u})+(\nabla \mathbf{u})^T)]-\nabla P=-\mathrm{Ra}_T T\hat{r}, \tag{2}$$

and

$$\frac{\partial T}{\partial t}=\nabla^2 T-\mathbf{u}\cdot\nabla T+\mathrm{H}, \tag{3}$$

respectively, where $\mathbf{u}$ is velocity, η is dynamic viscosity, P is the nonhydrostatic pressure, T is temperature, t is time, H is the nondimensional internal heating rate, and Ra_T is a reference Rayleigh number. The governing equations (1)–(3) have been nondimensionalized with the use of a thermal diffusion time scale. In addition $\eta=\bar{\eta}/\eta^*$, where $\bar{\eta}$ represents the dimensional field and η^* is a dimensional reference viscosity. We assume that mantle flow occurs by diffusion creep, a process by which atoms diffuse through the interiors of crystal grains under stress and/or along grain boundaries. Consequently, we model a linear relationship between stress and strain rate (Turcotte & Schubert, 2014). The spherical annulus geometry we employ yields solutions of the conservation equations in the equatorial cross section of a spherical shell with no variation in colatitude. Thus, upwelling and downwelling features in our calculations can be thought of as a crescent-like sheet of maximum thickness in the equatorial plane, that tapers until vanishing at the poles of the sphere (i.e., in a spherical geometry where the colatitude $\theta=\pi/2$ coincides with the plane of the annulus; a 3-D spherical harmonic decomposition of the solution obtained would have only sectoral harmonics; analogous to the segments in an orange).

The dimensional linearized equation of state

$$\rho=\rho_0(1-\alpha(T-T_0)) \tag{4}$$

is incorporated in the system of partial differential equations (1)–(3) so that our calculations implicitly assume that $\rho_0=\rho(T_0)$ corresponds to the surface density. This equation of state also introduces α, the thermal expansivity, appearing in the Rayleigh number, Ra_T.

The reference Rayleigh number is defined as:

$$\mathrm{Ra}_T=\frac{\rho_0 g\alpha\Delta T d^3}{\kappa\eta^*}, \tag{5}$$

where d is the thickness of the mantle, $\Delta T=[T_b-T_0]$ (where T_b is the isothermal basal temperature and T_0 is the isothermal surface temperature), g is gravitational acceleration, and κ is the thermal diffusivity.

The nondimensional viscosity value corresponding to η^* is 1. However, because the viscosity is a strong function of temperature, stress, and depth, it is insightful to define an effective Rayleigh number, specifically

Table 1
Dimensional Quantities Adopted for This Study When $Ra_T = 2\times10^8$

Quantity	Dimensional value
η^*	2.22×10^{20} Pa s
κ	10^{-6} m^2 s^{-1}
d	2.89×10^6 m
ΔT	2,500 K
Diffusion time, d^2/κ	265 Gyr
ρ_0	3,700 kg m^{-3}
g	10 m s^{-2}
α	2×10^{-5} K^{-1}
k	4.25 W m^{-1} K^{-1}

Note. The reference viscosity value is determined by all other values assigned to the parameters comprising Ra_T.

$$Ra_{eff} = \frac{Ra_T}{\eta_{avg}}, \tag{6}$$

where

$$\eta_{avg} = \frac{2}{4\pi/3(r^3_{surf} - r^3_{core})}\int_0^{2\pi}\int_{r_{core}}^{r_{surf}} \eta(r,\phi) r^2 dr d\phi \tag{7}$$

is the time-dependent spatially averaged nondimensional viscosity of the system, r_{core} is the radius of the core, r_{surf} is the radius of the surface of the spherical system, ϕ is the azimuthal angle, and r is spherical radius.

The nondimensional internal heating rate

$$H = \frac{\rho_0 \epsilon d^2}{k\Delta T}, \tag{8}$$

where k is the thermal conductivity and ϵ is the dimensional heating rate per unit mass (specified to be uniform throughout the mantle in this study).

Table 1 summarizes the dimensional values adopted for these quantities in this study. Given the values quoted in Table 1, the Rayleigh number, Ra_T, is approximately 2×10^8. This Rayleigh number is chosen because it yields vigorous convection for most of the cases explored in our study. It is consistent with a reference viscosity value of η^*. However, the feedback between viscosity and temperature results in an effective Rayleigh number, Ra_{eff} (determined by the average viscosity) that is 2–4 orders of magnitude less than Ra_T. Accordingly, the parameters specified in the viscosity laws used in our calculations result in mean nondimensional viscosities that are generally 2–4 orders of magnitude greater than 1 and values of Ra_{eff} that are 2–4 orders of magnitude less than 2×10^8.

2.2. Rheology

We obtain surface motion by supplementing a temperature-dependent rheology with viscoplastic yielding. Specifically, we implement a nondimensional Arrhenius-type law to model a nondimensional temperature-dependent rheology:

$$\eta_T = \exp\left(\frac{E_a}{T+1} - \frac{E_a}{2}\right), \tag{9}$$

where E_a is an effective nondimensional activation energy that determines the magnitude of the thermal viscosity contrasts. In this study, the thermal viscosity contrast, $\Delta\eta_T$, is fixed at values of either 3.2×10^5 or 3.2×10^6. This contrast is specified using the viscosity law given in equation (9) with E_a set to 25.35 or 29.96, respectively. Accordingly, the dimensional surface viscosity is set to 7.1×10^{25} Pa s or 7.1×10^{26} Pa s and is specified independently of the dimensional surface temperature.

A nondimensional yield stress is modeled using a two component paradigm where

$$\sigma_{yield} = \min\left[\sigma_{ductile}, \sigma_{brittle}\right] \tag{10}$$

defines a yield stress that can be specified to be depth-dependent. In all cases considered, $\sigma_{ductile}$ is the constant yield stress that (in practice) characterizes the mantle below the upper thermal boundary layer of the convecting systems and therefore contributes to determining the vertical gradient of the yield stress in the model lithosphere. The yield stress in the upper thermal boundary layer is given by $\sigma_{brittle}$. Equation (10) therefore allows us to emulate a Byerlee-type law for rock strength which results in a yield stress that increases with depth until reaching the ductile regime (Kennett & Bunge, 2008; Kohlstedt et al., 1995). To completely specify the yield stress in the brittle region of the uppermost mantle requires two parameters: the cohesion (μ) and μ' a value linearly proportional to the friction coefficient. The cohesion defines the surface value of yielding while the friction coefficient is determined by the specification of $\sigma_{ductile}$ and setting a depth for the base of the brittle region (discussed below). Accordingly, the brittle region of yielding is modeled with the following equation:

$$\sigma_{brittle} = \mu + (1-z)\mu', \tag{11}$$

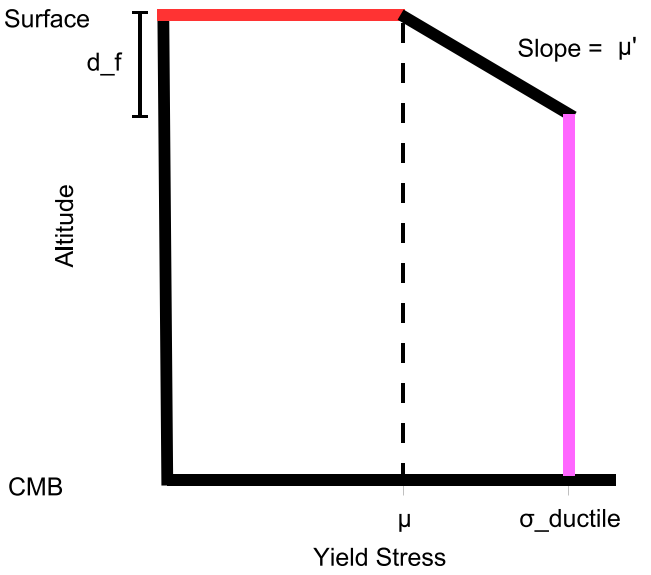

Figure 1. An example yield stress profile based on equations (10) and (11). The nondimensional thickness of the depth-dependent yield stress layer is d_f. The cohesion, μ, specifies the yield stress of the surface. The friction coefficient, μ', controls the rate of increase of yield stress with respect to depth and $\sigma_{ductile}$ is the constant yield stress of the lower 95–97.5% of the mantle, depending on the value of d_f.

where z is the nondimensional height above the CMB. In this study, transition from the (shallow) brittle region to a yield stress determined by ductile behavior is set at fixed depths. This is done by specifying $\mu' = d_f^{-1} \times (\sigma_{ductile} - \mu)$, where d_f^{-1} controls the transition depth. A d_f^{-1} value of either 20 or 40 is specified so that the upper 5 or 2.5% of the mantle (i.e., 1/20th or 1/40th of the depth) experiences a yield stress associated with brittle failure (although rock fracture does not occur explicitly in our models). This failure can result in reduced viscosity in regions of high stress. Figure 1 illustrates the variation in yield stress for a general case.

Plastic yielding is introduced into the solutions of equations (1)–(3) by the introduction of a yield viscosity that is related to the yield stress by the linear relationship:

$$\eta_{yield} = \frac{\sigma_{yield}}{2\dot{\epsilon}}, \tag{12}$$

where $\dot{\epsilon}$ is the second invariant of the strain rate tensor,

$$\dot{\epsilon} = \sqrt{\frac{1}{2}\dot{\epsilon}_{ij}\dot{\epsilon}_{ij}}. \tag{13}$$

Given this definition of yield stress, a spatially and temporally dependent composite viscosity, η_{comp}, can be calculated to account for the influence of temperature and stress-dependent rheologies, where

$$\eta_{comp} = \frac{1}{1/\eta_T + 1/\eta_{yield}}. \tag{14}$$

The presence of a significant pressure induced increase in viscosity with descent, from the upper to the lower mantle, accompanies the transition from a spinel phase to the perovskite-magnesiowustite structure (Bridgmenite) (Boehler, 2000). Numerous investigations of geophysical observables have inferred that mantle viscosity increases by a factor of 30 or greater at a depth coinciding with this phase transition (Hager, 1984; King & Masters, 1992; Mitrovica & Forte, 2004; Richards & Hager, 1984). Consequently, a lower mantle viscosity increase is specified for all calculations presented here, such that the nondimensional viscosity field $\eta = \eta_{comp} \times \eta_D$, where $\eta_D = 1$ for $z \geq 1 - 0.227$ and $\eta_D = 30$ for $z \leq 1 - 0.227$. In some calculations, we consider a larger increase in lower mantle viscosity at depths below $1 - 0.227$ (dimensional depth 660 km). In those cases when $\eta_D \leq 1 - 0.227$ is set equal to 100 the Rayleigh number, Ra_T, is altered to approximate similar convective vigor and effective Rayleigh number to cases where $\eta_D = 30$ in the lower mantle. Unless stated otherwise, a Rayleigh number Ra_T of 2×10^8 is specified.

Given the various influences on viscosity in our model, we also employ a measure of the convective vigor of the systems determined by an internal Rayleigh number:

$$\mathrm{Ra}_{int} = \frac{Ra_T}{\eta_T(\bar{T}_{mid})\overline{\eta_D}}, \tag{15}$$

where $\eta_T(\bar{T}_{mid})$ is the thermal viscosity corresponding to the temperature at midmantle depth and $\overline{\eta_D}$ is the mean nondimensional value of mantle viscosity in the absence of thermal or stress-dependent effects. When $\eta_D = 30$ or 100, $\overline{\eta_D}$ has values of 20.30 and 66.90, respectively.

2.3. Thermochemical Convection

Seismic imaging of the lower mantle (Lekic et al., 2012; Ritsema et al., 2011; Simmons et al., 2010) indicates the presence of a rich variety of density anomalies. Beneath the Africa and Pacific plates, within and extending above the D″ region, are the Large Low-Shear Velocity Provinces (LLSVPs). The LLSVPs have been inferred to be compositionally distinct material with a chemistry that differs from the ambient mantle (Lekic et al., 2012; Masters et al., 2000). Given their possibly distinct chemical nature and residence near the base of the mantle it is typically assumed that LLSVPs are intrinsically dense.

For a small subset of calculations, we model a mantle composed of both ambient silicate material as well as inherently dense material. Thermochemical convection is modeled by solving the nondimensional equations (1) and (3) for mass and energy conservation, respectively, as well as an equation for advection of the composition field and an augmented equation for momentum conservation that accounts for the effect of compositional buoyancy,

$$\frac{\partial C}{\partial t} = -\mathbf{u} \cdot \nabla C \tag{16}$$

and

$$\nabla \cdot [\eta(\nabla \mathbf{u}) + (\nabla \mathbf{u})^T)] - \nabla P = (-\mathrm{Ra}_T T + \mathrm{Ra}_C C)\hat{r}. \tag{17}$$

In equations (16) and (17), C is the composition field and Ra_C is the compositional Rayleigh number,

$$\mathrm{Ra}_C = \frac{\Delta\rho_C g d^3}{\kappa \eta *}, \tag{18}$$

where $\Delta\rho_C$ is the compositional density contrast between the enriched and ambient material. For a given fraction C of enriched material, the dimensional density, $\rho(T)$ (see equation (4)) is increased by adding $C\Delta\rho_C$. The maximum departure from the reference density due to compositional versus temperature effects is given by the buoyancy ratio, $B = \Delta\rho_C/(\rho_0 \alpha \Delta T)$, (equivalent to $\mathrm{Ra}_C/\mathrm{Ra}_T$).

In this study, we specify a buoyancy ratio of either 0.7 or 1.0 to model thermochemical convection, implying a dimensional density increase of 115 kg/m^3 or 185 kg/m^3, respectively, when $C = 1$. The compositional field is initiated as a layer enveloping the core-mantle boundary with a prescribed volume of 3.5 or 5% of the associated spherical shell. The tracer ratio method (Tackley & King, 2003) is employed to solve equation (16), where tracer particles are used to track the location of compositionally distinct material. We use an average of 32 tracers per grid cell to track the compositional field.

2.4. Model Analysis and Output

Through the variation of yield stress, nondimensional internal heating rate, thermal viscosity contrast, and the ratio of upper to lower mantle viscosity, we investigate surface velocity and the requirements for plate-like surface motion in a suite of mantle convection models. The relevance of our findings to terrestrial mantle convection is assessed by considering the temporally averaged ratio of core to surface heat loss as well as time-averaged statistics that quantify the nature of the surface velocity field. All model statistics reported are obtained by integrating our calculations for time periods in excess of 10 transit times once a statistically steady state has been obtained (i.e., a state in which long-term heating or cooling is absent).

A model naming convention has been adopted throughout the remainder of this paper. The model names generally follow the format HhhYyyy(Ta), where hh is the model's nondimensional internal heating rate and yyy is the ductile yield stress, $\sigma_{ductile}$. However, some cases are not uniquely identified by their internal heating rate and the ductile yield stress. Thus, Ta is a number corresponding to the Table found in the supporting information in which all parameters are listed, specific to the model referenced (e.g., Model H30Y1e7(2) is described in the supporting information Table S2, and other cases which feature H = 30 and $\sigma_{ductile} = 10^7$, but have different parameters, appear in different tables). When cohesion values are varied we state the unique cohesion value of each Model. Unless specified, $\mu = 0$ for all calculations. In addition, unless noted otherwise in the table where a model is listed, all calculations feature a lower mantle viscosity increase, η_D, of 30; a thermal Rayleigh number, Ra_T, of 2×10^8; $d_f = 0.05d$ and a thermal viscosity contrast, $\Delta\eta_T$, of 3.2×10^5. Thermochemical convection calculations are identified by model names in the format ThermoBbbVvv(4), where bb is the buoyancy ratio, vv is the percentage of the volume composed of intrinsically dense material and (4) indicates that the Thermochemical convection cases are listed in the supporting information Table S4.

An $f = r_{core}/r_{surf}$ ratio of 0.547 is specified in all calculations, so that the ratio of the core radius to the planet radius is the same mean as for the Earth. Free-slip as well as isothermal surface and core boundary conditions are used and the surface and core-mantle boundary (CMB) nondimensional temperatures are set to $T = 0.0$ and $T = 1.0$, respectively.

The percentage of the total surface heat loss that arises from core heat loss is measured by computing

$$PCH = f^2 \frac{q_{core}}{q_{surf}}, \tag{19}$$

where q_{core} and q_{surf} are the mean nondimensional core and surface heat fluxes, respectively. In the remainder of this paper, we refer to the quantity calculated by (19) as the percentage of core heating, where the values quoted are temporally averaged. It should be noted that equation (19) is only valid when the right-hand side is a temporally averaged quantity. Specifically, it is valid when averaged over time periods for which

$$q_{surf} - f^2 q_{core} = (1 + f + f^2)H/3. \tag{20}$$

The left-hand and right-hand sides of this equation differ by no more than 2% for the time periods over which averaging is done for the calculations we report.

In order to classify the convective regime, the mobility, M, is considered, as in many previous studies (e.g., Foley & Becker, 2009; Stein et al., 2014; Tackley, 2000a; van Heck & Tackley, 2008). Mobility is defined as the ratio of the surface root-mean-square velocity (v_{rms}) to the root-mean-square velocity of the entire convecting system (V_{RMS}), thus

$$M = \frac{v_{rms}}{V_{RMS}}. \tag{21}$$

Very small mobility (i.e., $M \ll 1$) defines the stagnant-lid regime (Moresi & Solomatov, 1995).

In the presence of yielding, focused surface deformation can occur. On a planet featuring plate-tectonic-like surface motion, surface deformation occurs primarily along narrow, confined plate boundaries. Conversely, plate interiors experience little to no deformation. Accordingly, we calculate the plateness, P, a parameter used to measure the localization of surface deformation and quantify the manifestation of plate-tectonic-type surface motion. Similar to previous studies (Tackley, 2000a; van Heck & Tackley, 2008) we define the plateness as:

$$P = 1 - \frac{f_{80}}{0.5}, \tag{22}$$

where f_{80} is the fraction of the surface area where the highest 80% of surface deformation takes place. The surface deformation is measured by the second invariant of the strain rate tensor:

$$\dot{\epsilon}_{surf} = \sqrt{\dot{\epsilon}_{xx}^2 + \dot{\epsilon}_{yy}^2 + 2\dot{\epsilon}_{xy}^2}. \tag{23}$$

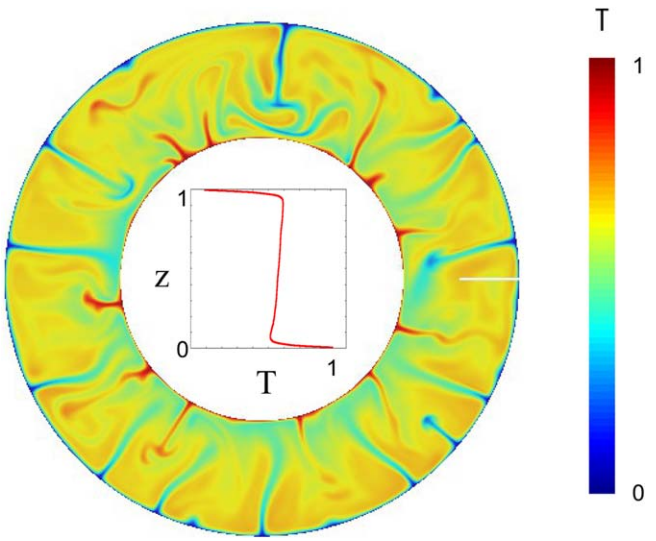

Figure 2. Nondimensional temperature field corresponding to isoviscous Model H30Y1e7iso4. A radially averaged temperature profile is presented that plots nondimensional altitude (z) versus temperature (T). A temperature color scale is included that ranges from a nondimensional temperature of 0 to 1.

The plateness is scaled to cases with isoviscous mantles which yield an f_{80} value of approximately 0.5. This definition ensures that systems with a plateness greater than zero feature surface fields where the greatest deformation is confined to narrower zones than an isoviscous case. A plateness of 1.0 is indicative of perfect plates (i.e., vanishingly small plate boundary width and near zero strain rate in plate interiors).

The scaling factor of 0.5 in equation (22) was determined from an isoviscous analog to Model H30Y1e7(2) (described in section 3.1). However, a reference Rayleigh number in the isoviscous case comparable to the effective Rayleigh number of Model H30Y1e7(2) does not yield similar convective vigor in the two cases, as determined by system V_{RMS} and q_{surf}. The reference Rayleigh number for the isoviscous case was increased until matching the V_{RMS} of Model H30Y1e7(2). In all cases examined f_{80} remains approximately equal to 0.5. Supporting information Table S5 gives the effective Rayleigh number, f_{80}, P, V_{RMS}, and PCH values for Model H30Y1e7(2) and the isoviscous analog cases. A temperature snapshot from Model H30Y1e7iso4 is presented in Figure 2 and is accompanied by a radial profile of temperature for later comparison to calculations with more complex rheologies. The profile depicts a model with relatively uniform temperatures throughout the upper and lower

mantle. A comparison of Ra_{eff}, q_{surf}, and V_{RMS} values in the supporting information Table S2 indicates that our calculations featuring complex rheologies yield effective Rayleigh numbers at least an order of magnitude lower than isoviscous convection cases of comparable vigor. Accordingly, neither Ra_{eff} nor Ra_{int} values are indicative of convective vigor or boundary layer thickness based on scaling derived from isoviscous calculations.

2.5. Initial Conditions

Figure 3 displays snapshots of the temperature and viscosity field used for starting nonisoviscous calculations (a snapshot taken from Model H30Y2e6(2)) as well as the associated time series of mobility, plateness, heat flux, and PCH. This initial condition was obtained by intermittently adjusting the Rayleigh number and yield stress in a calculation started from a randomly perturbed conductive temperature field in a spherical annulus. The nondimensional heating rate and η_D were fixed during the variation of the above mentioned parameters. The viscosity contrast due to temperature, the yield stress and the Rayleigh number were adjusted upward incrementally in order to obtain an initial condition system characterized by a time-

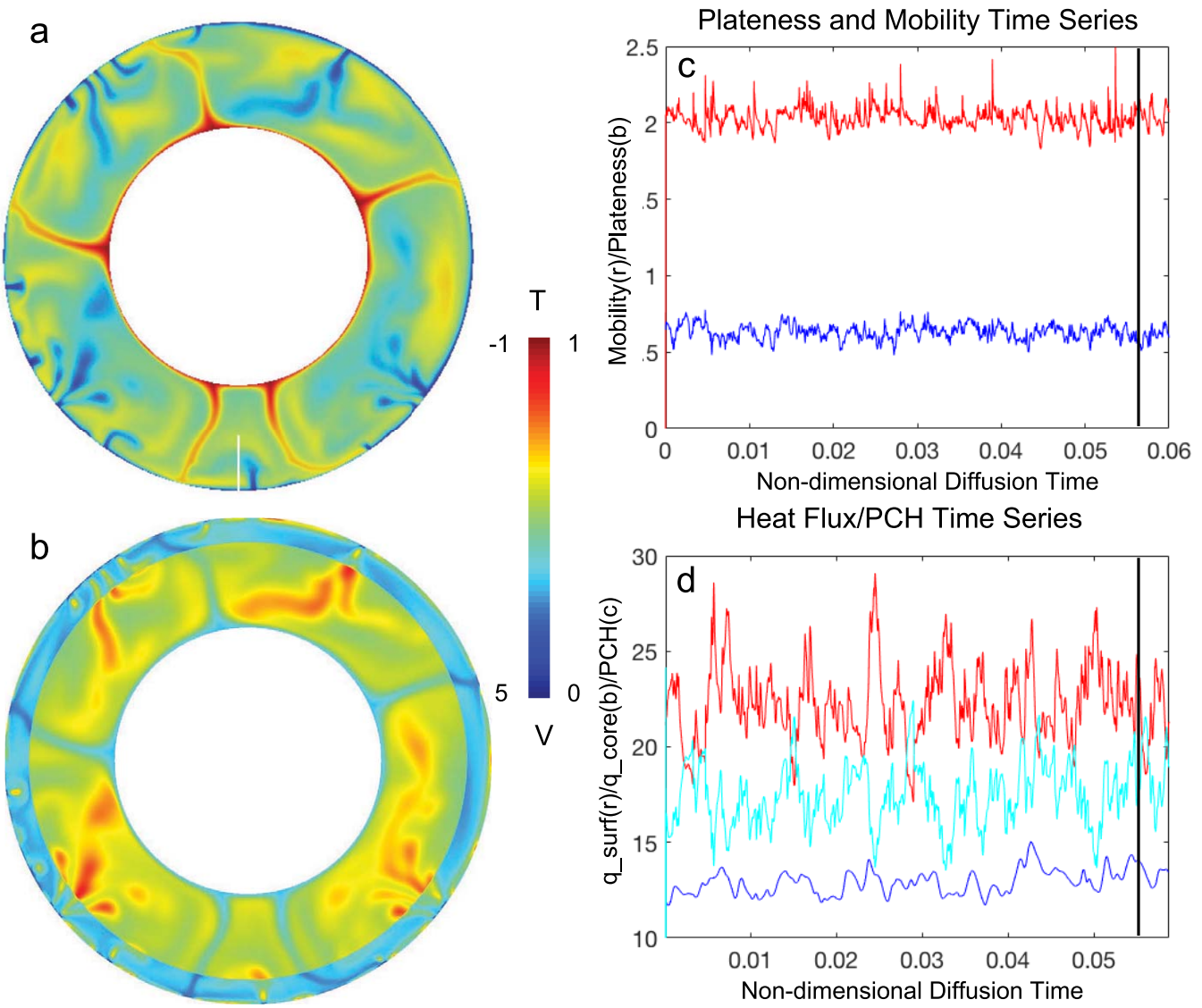

Figure 3. Initial conditions: (a) nondimensional temperature field and (b) viscosity field. (c) Mobility (red) and plateness (blue) time series. (d) Nondimensional basal (blue) and surface (red) heat flux time series as well as PCH (cyan). The parameters specified in the calculation are $Ra_T = 2\times10^8$, $\Delta\eta_T = 3.2\times10^5$, H = 30, $\sigma_{ductile} = 2\times10^6$, $\mu = 0$, and $d_f = 0.05$. The black vertical lines in Figures 3c and 3d indicate the time corresponding to the temperature and viscosity field snapshots. A nondimensional period of 0.1 corresponds to a dimensional period of 2.6 billion years.

averaged mobility greater than 1.0 and a PCH below 25% (the final PCH value obtained was 20.5% with the parameters specified for the initial condition). In addition, we focused on obtaining strong plateness and limiting the effective Rayleigh number to a value that could be accurately modeled. Throughout the search for an initial condition, we avoided changing model parameters to values that would drive the system into the stagnant-lid regime. The resolution of the calculations is given in corresponding table captions.

Previous work has described the sensitivity of convective regime to initial conditions, and specifically that more than one statistically steady convective solution can exist for a given set of model parameters, where the solution is dependent on the initial condition (e.g., Lenardic & Crowley, 2012). For example, in a suite of calculations that systematically reduce yield stress, the transition from a stagnant-lid regime to a mobile surface mode occurs at a different critical yield stress than that which allows for the onset of stagnant-lid convection when yield stress is gradually increased in initially mobile surface cases (Lenardic & Crowley, 2012; Weller & Lenardic, 2012). This affect is now often described in the mantle convection literature as hysteresis. In order to ensure reproducible results, in this study we control the hysteresis affect by starting all calculations using Model H30Y2e6(2) (unless explicitly described otherwise). Consequently, all calculations begin with a mobile surface. In order to explore the influence of a variety of factors a one-time change of an input parameter (e.g., nondimensional internal heating rate, H, ductile yield stress, $\sigma_{ductile}$, etc.) occurs when starting calculations from the initial condition. In the event that a one-time parameter change leads to issues with numerical convergence, the parameter will then be scaled up incrementally. For example, increasing the thermal viscosity contrast by one order of magnitude from our initial condition requires taking several small step increases in viscosity contrast in order to maintain solution stability.

3. Results

3.1. The Effect of Yield Stress Magnitude

The definition of the yield stress given by equations (10) and (11) ensures that the brittle yield stress is determined by setting the ductile value and the cohesion. In the remainder of this paper, where we refer to a yield stress without reference to a depth, the yield stress described should be considered the ductile value.

Figure 4 shows a sequence of thermal field snapshots and temporally averaged statistics for a suite of calculations in which $\sigma_{ductile}$ is systematically increased. In the lowest yield stress case, a vertical velocity profile indicates the presence of layering as the majority of cold material stagnates in the upper mantle. As yield stress is increased, vertical velocity profiles indicate that downwellings are far less impeded by the presence of a lower mantle viscosity increase. The abundance of weak downwellings in the first case is a consequence of weaker yield stresses and numerous locations where yielding is obtained. Multiple sites of downwelling formation keep the system cool so that upwellings are vigorous and the dominant influence on convective wavelength. The PCH is between 17% and 18%.

For yield stresses of 10^7 and 2×10^7 downwellings become much more focused and negatively buoyant than in the cases with lower yield stresses. This behavior can be seen in the Figure 4 snapshots from Models H30Y1e7(2) and H30Y2e7(2). These cases also exhibit higher plateness. A threshold exists for yield stresses between 2×10^7 and 3×10^7 where plateness begins to drop and mobility becomes much more variable. This behavior marks the onset of an episodic mobility regime, characterized by short-lived downwellings, higher degree upper mantle convection, warmer interiors, and a decline in PCH. For values of $\sigma_{ductile} \geq 10^8$, the calculations are dominated by degree 1 convection. As yield stress is increased to a nondimensional value of 1×10^9, a near stagnant-lid regime is obtained, resulting in a great reduction in plateness as well as producing heat flow into the core from the internally heated mantle.

The mobile regime corresponds to models with both plate-like and nonplate-like surfaces. The latter cases are distinguished by a mobility value, M, greater than 2.0 and the presence of multiple short-lived drips in the upper mantle. Conversely, plate-like models possess a mobility less than 2.0 and feature longer wavelength convection. We find approximately two orders of magnitude in yield stress span a regime of behavior, often identified as episodic or transitional, prior to the onset of sluggish lid. A full three orders of magnitude separate yield stresses characterizing the nonplate-like mobile regime (Model H30Y5e5(2)) from yield stresses at which the stagnant-lid regime appears (Model H30Y1e9(2)).

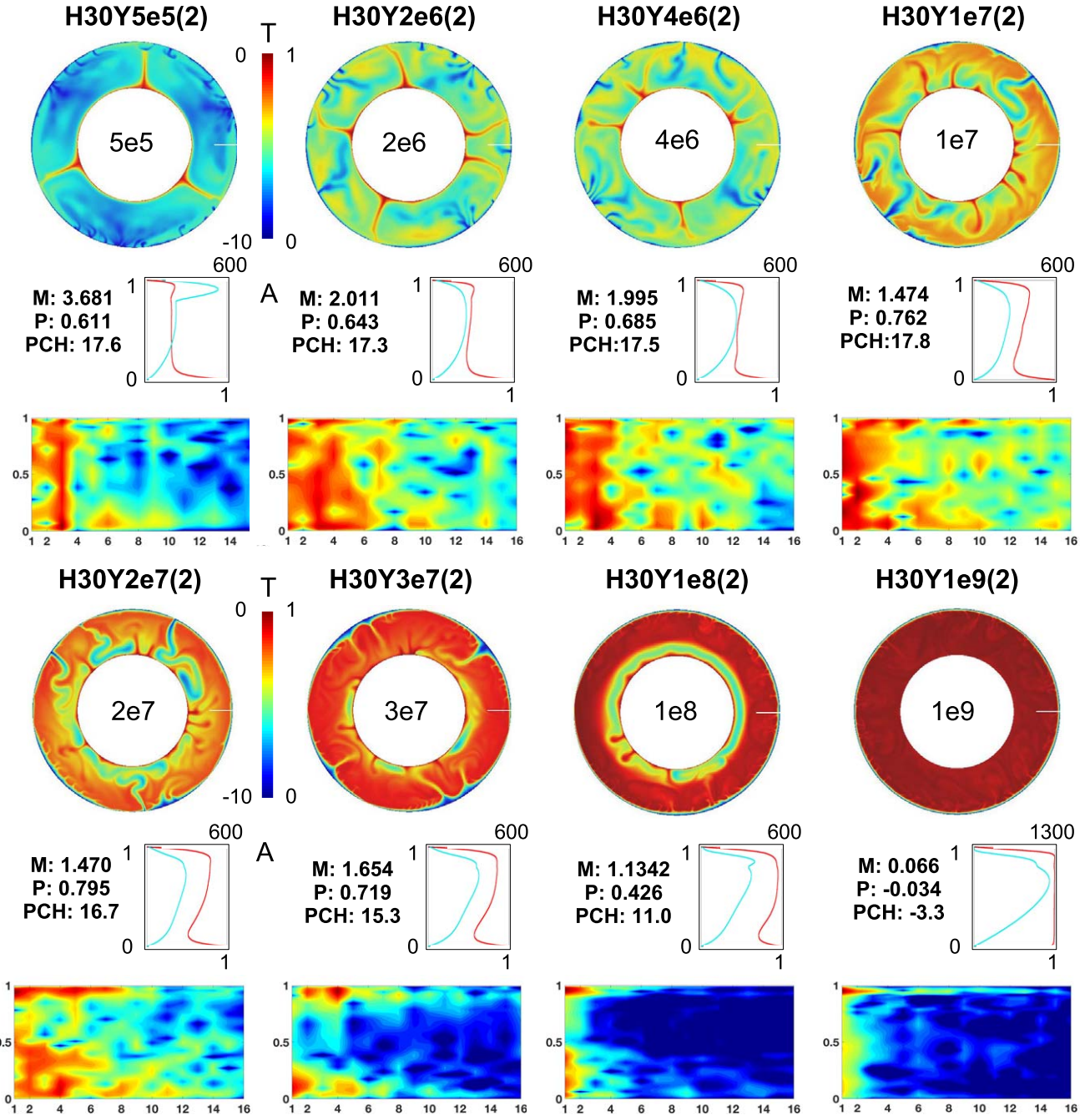

Figure 4. Temperature field variation as a function of yield stress ($\sigma_{ductile}$). Model identifiers (appearing in supporting information Table S2) are given above annulus images of the temperature field. The second figure from the left (top row) corresponds to the initial condition shown in Figure 3. Values of temporally averaged plateness, P, mobility, M, and percent-core-heating (PCH) are given for each case below the temperature field snapshots. Temperature field power spectra (plotted as altitude versus power) and profiles of the laterally averaged temperatures (red) and vertical velocities (cyan) (plotted as altitude versus temperature) are placed below and beside the M, P, and PCH values for each plot respectively. A color-bar, located next to the left most model on each line, indicates both the nondimensional temperature (right scale) and the logarithm of the amplitude of the power spectra (left scale).

3.2. Effects of Internal Heating Rate

Figure 5 presents a suite of snapshots from calculations featuring a range of internal heating rates, and yield stresses of 2×10^6 or 1×10^7. The cohesion value $\mu = 0$ in all cases. Multiple downwellings are present in all calculations but increase in number while decreasing in longevity as H is increased (e.g., compare Model H30Y1e7(2) to Model H60Y1e7(3) to Model H90Y1e7(3)). Consequently, downwelling formation becomes more episodic as H increases. Our finding is consistent with van Hunen and van den Berg (2008) who also

10.1002/2017GC007266

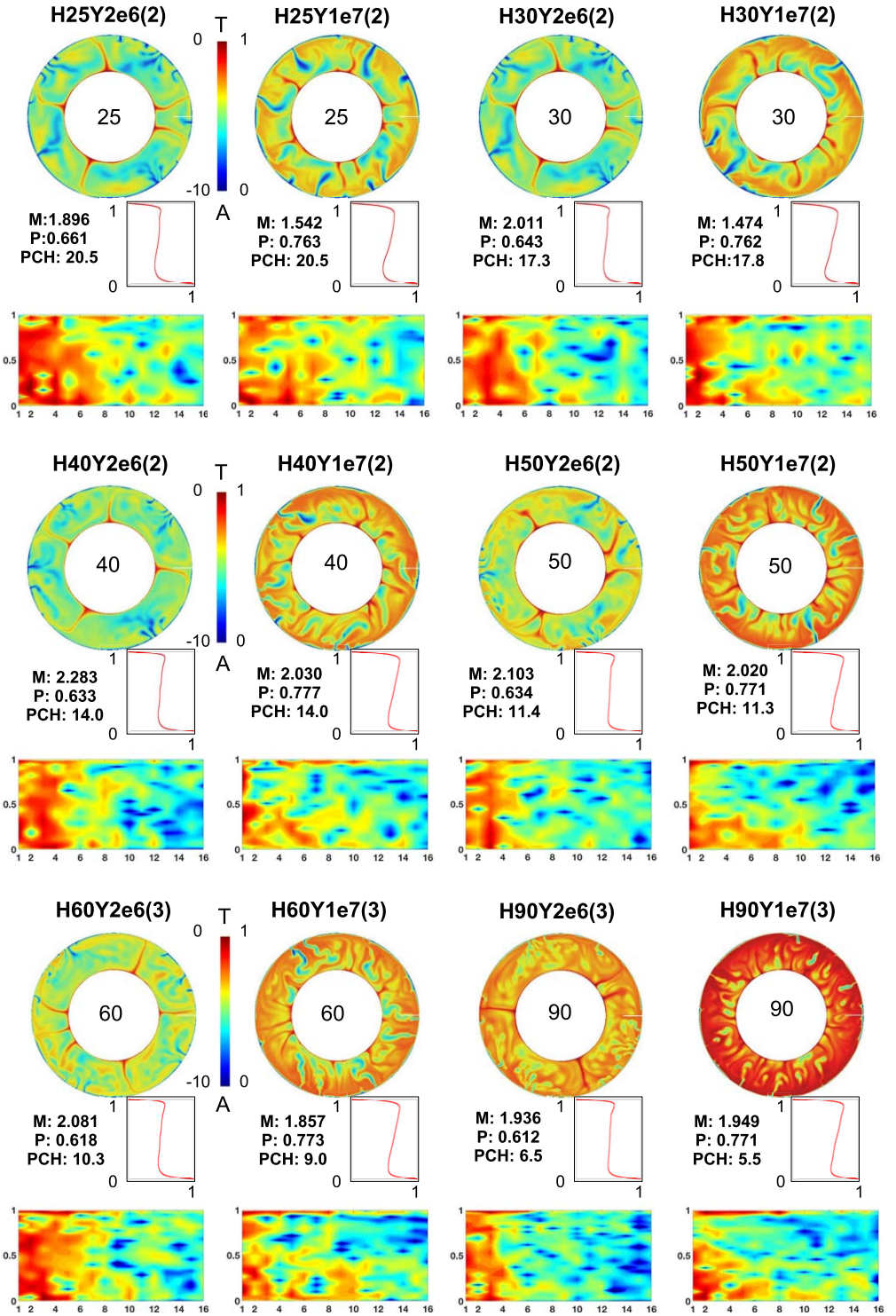

Figure 5. Temperature field variation as a function of internal heating rate for two yield stress values ($\sigma_{ductile}=2\times10^6$ and 10^7). Model identifiers from the supporting information Tables S2 and S3 are given above each annulus image. The third plot in the top row corresponds to the initial condition case shown in Figure 3. Values of temporally averaged plateness, P, mobility, M, and percent-core-heating (PCH) are given for each case below the temperature field snapshots. Temperature field power spectra (plotted as altitude versus power) and profiles of the laterally averaged temperatures (plotted as altitude versus temperature) are placed below and beside the M, P, and PCH values for each plot, respectively. A color-bar, located next to the left most model on each line, indicates both the nondimensional temperature (right scale) and the logarithm of the amplitude of the power spectra (left scale).

found that slab break-off becomes more common and subduction more transient when mantle temperatures are increased. Variations in internal heating rate do not produce a systematic trend in mobility for $25 \leq H \leq 90$. Similarly, for the Ra_T employed here, the internal heating rate has negligible impact on plateness, particularly for the higher yield stress calculations.

In Figure 6a, we plot the PCH versus the yield stress for calculations featuring two different internal heating rates. Yield stress increase has minimal effect on PCH for cases that remain mobile but PCH decreases monotonically with yield stress with the onset of the transitional (episodic) regime. In contrast, Figure 6b plots the PCH against internal heating rate for cases with yield stress 2×10^6 and 10^7. PCH declines steadily as H is increased for both yield stresses while all cases remain mobile. The influence that internal heating rate has on plateness and mobility, over the H range considered, is shown in Figure 6c, and indicates negligible sensitivity of the plateness statistic to internal heating rate while M varies weakly and nonsystematically.

Figure 7 shows mobility as a function of yield stress for a variety of calculations with different nondimensional internal heating rates. High variations in mobility are indicated by the cases with large standard

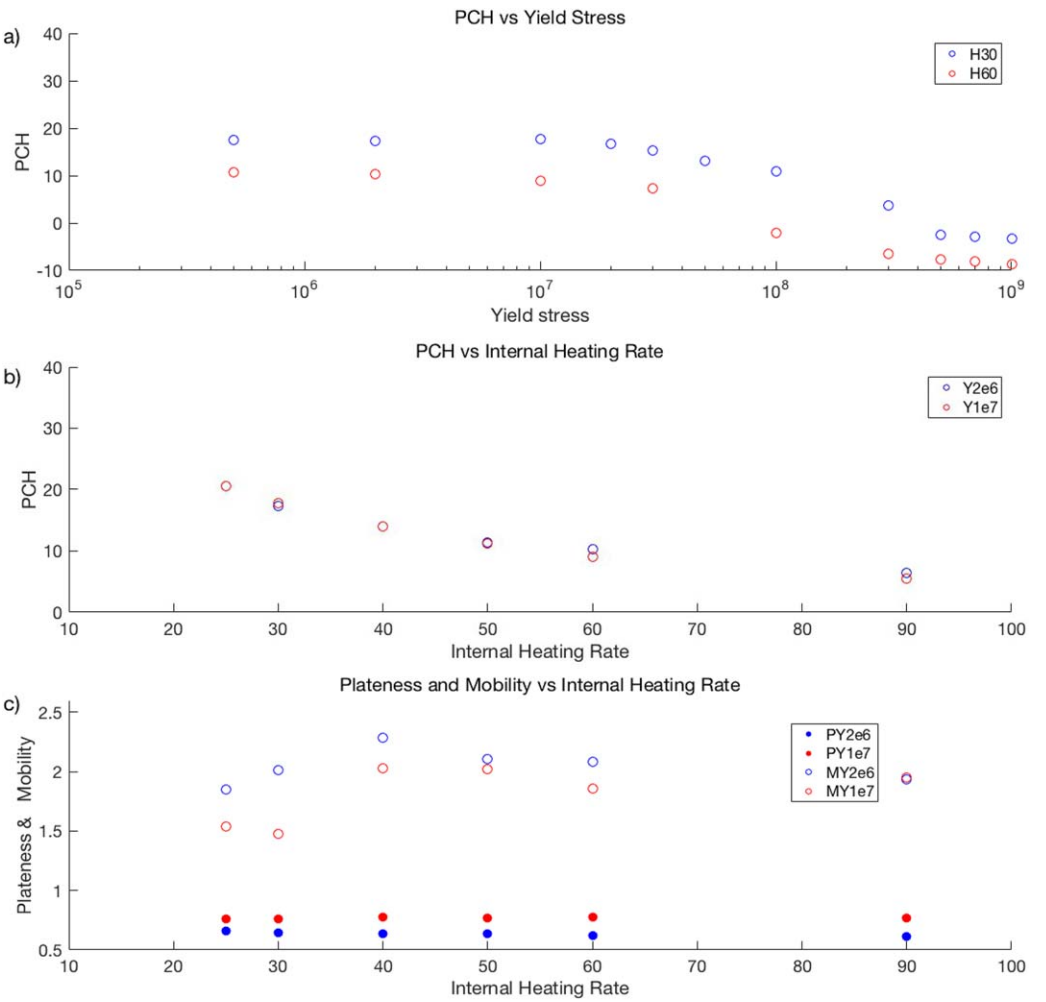

Figure 6. (a) Temporally averaged core heating (PCH) plotted against yield stress, $\sigma_{ductile}$ for internal heating rates of H = 30 and 60 using blue and red circles, respectively. (b) Temporally averaged percentage core heating (PCH) plotted against internal heating rate, H, for yield stresses $\sigma_{ductile}=2\times10^6$ and 10^7 using blue and red circles, respectively. For all models $\Delta\eta_T=3.2\times10^5$, $\mu = 0$, and $d_f = 0.05$. (c) Temporally averaged plateness and mobility plotted against internal heating rate. Plateness is plotted against internal heating rate, H, for calculations featuring yield stresses $\sigma_{ductile}= 2\times10^6$ and 10^7 using blue and red filled circles, respectively. Mobility is plotted against internal heating rate for yield stress 2×10^6 and 10^7 using blue and red empty circles, respectively.

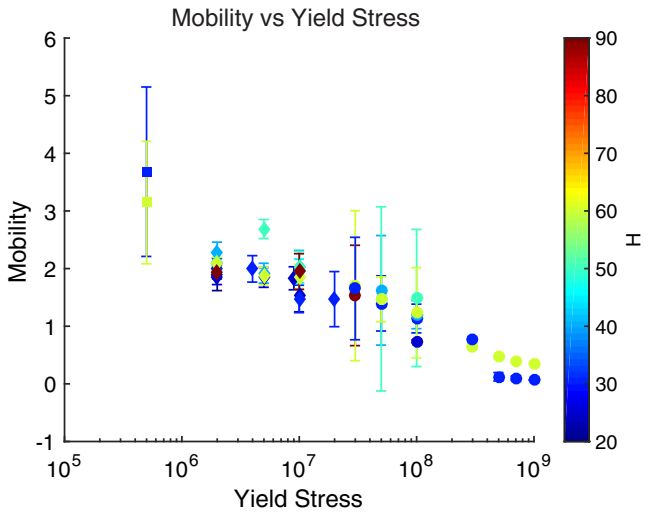

Figure 7. Mobility plotted as a function of yield stress ($\sigma_{ductile}$) for calculations featuring different nondimensional internal heating rates, H. Data-point colors indicate the value of H as indicated by the color-bar. Vertical bars indicate the standard deviation (in each case) resulting from time-dependence. Data-point shapes indicate the convective regime. Squares, diamonds and circles represent the mobile, plate-like and episodic/stagnant regimes of convection respectively, where plate-like models, with yield stress between 10^6 and 10^7, possess internal heating rates between 30 and 90. In all cases $\Delta\eta_T = 3.2\times10^5$, $\mu = 0$, $d_f = 0.05$. Model parameters can be found in the supporting information Tables S2 and S3.

deviations. For yield stresses of 5×10^7 and 10^8; the large standard deviation in mobility is due to the episodic behavior of convection. For example, Model H30Y1e8(2) (see Figure 4) experiences intermittent surface yielding resulting in the subduction of a large volume of cold material. This material descends into the interior of the mantle followed by the downwelling region receding and subsequently vanishing. Between each such event, a stagnant-lid forms for a short time, before stresses localize and produce a new convergent zone in the upper thermal boundary layer. For yield stresses of 5×10^5, the large standard deviation in mobility is due to the continuous formation (permitted by a low threshold for failure) and destruction of regions of focused convergence resulting in a highly time-dependent surface velocity. In summary, Figure 7 illustrates that there is a range of yield stresses for which mobility experiences minimal variations and we do not find that this range is particularly sensitive to the internal heating rate. This same region of yield stress range corresponds to models exhibiting the highest values for plateness.

Figure 8 shows plateness as a function of yield stress for a variety of calculations with different nondimensional yield stresses, $\sigma_{ductile}$. In all cases, the cohesion $\mu = 0$ and the thickness of the layer associated with brittle failure, d_f, is 0.05. Circles and diamonds now indicate calculations performed with reference Rayleigh numbers of 2×10^8 and 1×10^9, respectively. The color of each point indicates the internal heating rate used in that particular case. A clear peak in plateness occurs when $\sigma_{ductile} = 2\times10^7$ for Rayleigh number 2×10^8 calculations while increasing the Rayleigh number leads to a greater yield stress corresponding with peak plateness. Plateness does not indicate a clear sensitivity to internal heating rate, but does clearly drop substantially for yield stresses that result in episodic mobility for any heating rate.

Figures 9a and 9b summarize the impact that yield stress and internal heating rate have on both the percentage of the surface heat coming from the core and the total core heat flux, q_{core}. The percentage of heat from the core and the raw nondimensional heat flux from the core (PCH and q_{core}, respectively) are indicated by the color of the data points. Additionally, the data points are denoted as squares, diamonds, and circles indicating the convective regime; nonplate-like mobile ($P \leq 0.7$ and standard deviation of mobility $\geq \pm 0.3$), plate-like and episodic/stagnant, respectively. Vertical trends indicate a clear decrease in PCH with increasing internal heating rate, as expected, however the convective regime is not affected by the value of H for the range of internal heating rates examined. Despite the decrease in PCH as H increases in the mobile (including plate-like) regime, q_{core} does not diminish substantially. However, in the stagnant-lid regime both PCH and q_{core} diminish as H is increased. Horizontal trends indicate that yield stress has a substantial impact on convective regime but that for a given H, the PCH changes minimally within each convective regime. The substantial changes in PCH that do occur as yield stress is changed, occur where the transition to stagnant-lid convection sets in. It should be noted that for the Rayleigh number employed here (2×10^8), only a small number of cases are represented where episodic mobility becomes common in the intervening space between the plate-like and stagnant-lid regimes. When yield stresses are $2-3\times10^7$ and H is greater than 30, these systems present modeling challenges owing to the enormous temperature and viscosity gradients that result from the onset of new "subduction" into very hot interiors.

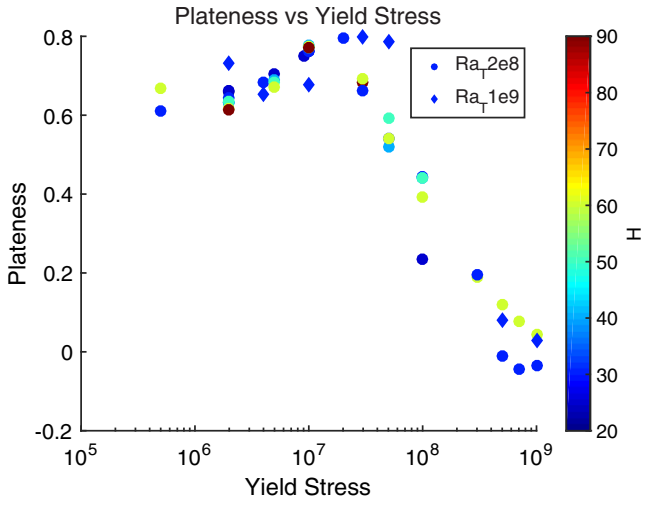

Figure 8. Plateness plotted as a function of yield stress ($\sigma_{ductile}$) for calculations featuring different nondimensional internal heating rates, H. Data-point colors indicate the value of H as indicated by the color-bar. Circles and diamonds correspond to models with Rayleigh numbers of $Ra_T = 2\times10^8$ and 10^9, respectively. Standard deviation is not shown due to its small magnitude. In all cases $\Delta\eta_T = 3.2\times10^5$, $\mu = 0$, and $d_f = 0.05$ (for $Ra_T = 2\times10^8$) or 0.025 (for $Ra_T = 10^9$). Model parameters can be found in the supporting information Tables S2, S3, and S7.

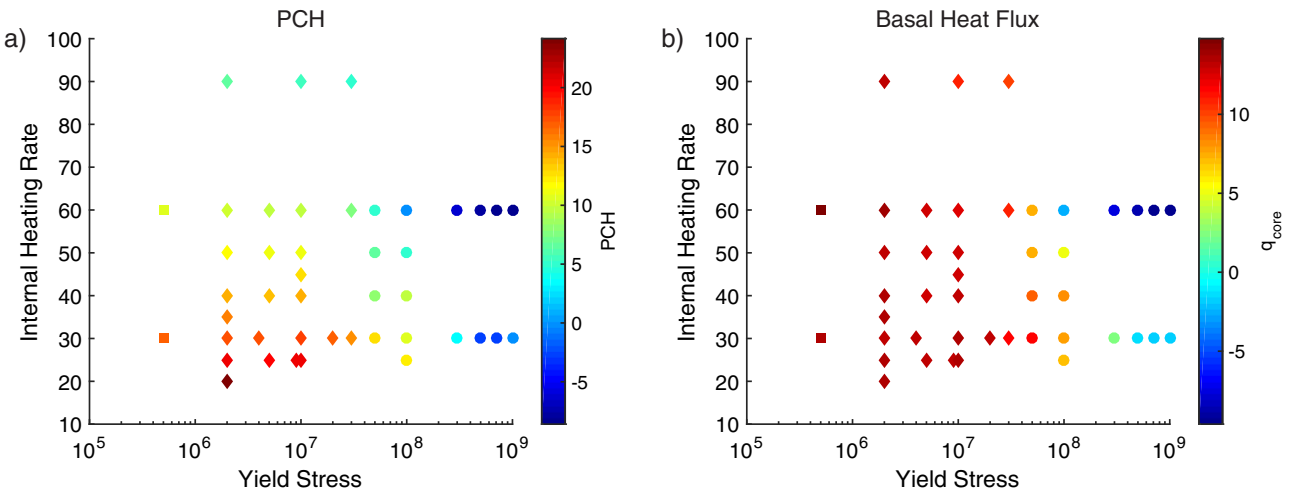

Figure 9. (a) Regime diagram showing the effect that variations in yield stress, $\sigma_{ductile}$ (x axis) and internal heating rate, H (y axis) have on the percentage of surface heat loss owing to core heat flow (PCH). Data-point colors indicate the percentage of surface heat flow resulting from core heating indicated by the color-bar. Squares, diamonds and circles indicate the mobile, plate-like and transitional/sluggish-lid regimes respectively. (b) Analogous to part (a), but instead data-point colors now indicate the nondimensional basal heat flux, q_{core}. Model parameters can be found in the supporting information Tables S2 and S3.

3.3. Effects of Lower Mantle Viscosity Increase

The influence of lower mantle rheology on plateness was investigated by increasing the contrast in viscosity at a depth of 660 km. The viscosity structure of the new model is obtained by effectively lowering the upper mantle viscosity by increasing Ra_T (by a factor of 2.5). Simultaneously, η_D is increased to 100 in the lower mantle (a factor of 3.33 relative to previous calculations). The net change in lower mantle viscosity is therefore an increase of 3.33/2.5 = 1.33 in the absence of the temperature-dependent or yielding influence on viscosity. The volumetrically averaged mean nondimensional viscosity of the mantle is increased by a factor of 1.02 due to the prescribed changes in Ra_T and η_D. Accordingly, relative to previous calculations, the specified Rayleigh number in the absence of thermal yielding effects is changed minimally in these cases when compared to previous calculations. Results are summarized in the supporting information Table S6. A snapshot from Model H30Y2e6(6) featuring a lower mantle viscosity increase of η_D=100, is shown in Figure 10, and demonstrates the influence of an increase in the intrinsic lower mantle viscosity from a factor of 30 to a factor of 100. The increase in lower mantle viscosity has minimal effect on the number of upwellings or dominant wavelength of convection in the lower mantle but influences convection in the upper mantle, which now exhibits layering (e.g., see Figure 10 velocity profile). Specifically, although the number of locations where the lithosphere yields is not reduced, many associated downwellings do not penetrate the 660 km boundary. However, downwellings coalesce in some locations where they manage to penetrate the 660 km boundary, broaden and become more diffuse. Overall, the presence of persistent downwellings descending to the CMB is reduced (e.g., when compared to the second plot of Figure 4). Consequently, slightly less heat is drawn from the core and the PCH is reduced.

In Figure 11a, we plot plateness and mobility against yield stress ($\sigma_{ductile}$) for cases with an intrinsic depth-dependent viscosity contrast of 30 and 100 (with H = 30). The viscosity change has a minimal effect on the time-averaged plateness and small effects on mobility but high mobility is maintained for greater yield stress when the contrast between lower and upper mantle viscosity is increased.

3.4. The Effect of an Increase in Rayleigh Number

To determine the significance of the influence of convective vigor on surface velocities (as well as thermal boundary layer thickness and plume conduit dimensions), we examined the influence of increasing Ra_T. Findings from these calculations are plotted in Figure 11b, where model results with varying yield stresses are compared for input Rayleigh numbers of 2×10^8 (with d_f=0.05) and 1×10^9 (with d_f=0.025). In all cases $\Delta\eta_T=3.2\times10^5$ (supporting information Table S7). Mildly higher (e.g., 0.05–0.2 greater) plateness occurs at higher yield stresses (e.g., 3×10^7 and 5×10^7) with an increased Rayleigh number. This observation is likely explained by a focusing of (greater) stresses into narrower regions of the model lithosphere as Rayleigh

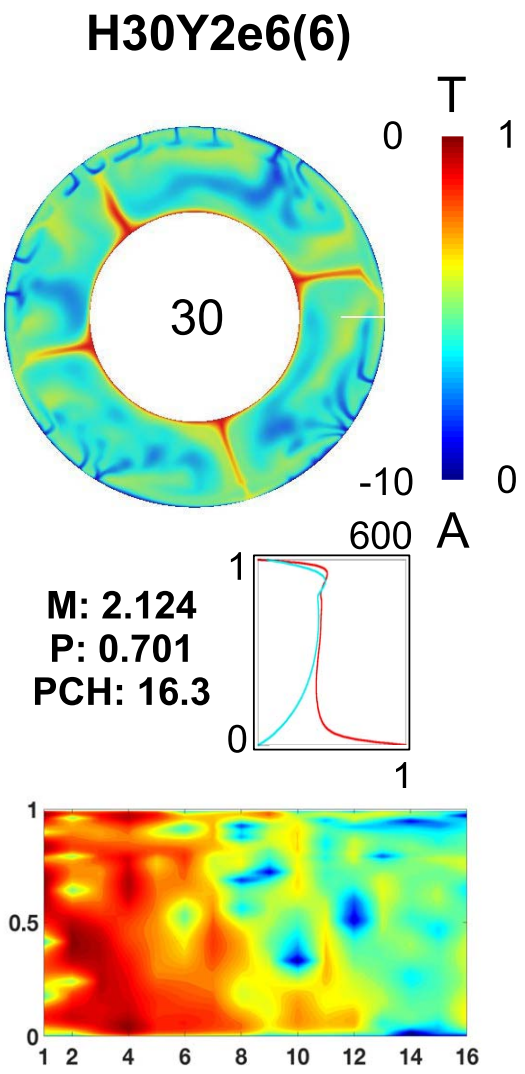

Figure 10. A calculation with an increased lower mantle viscosity (by a factor of 100 relative to the upper mantle), input Rayleigh number of $Ra_T = 5 \times 10^8$ and depth-dependent yield stress layer thickness of $d_f = 0.025$. Below the temperature field are time-averaged values for mobility, M, plateness, P, and percent-core-heating (PCH) as well as radially averaged temperature and vertical velocity profiles plotted in red and cyan, respectively (plotted as altitude versus temperature/vertical velocity). The bottom most image represents the temperature power spectra (plotted as altitude versus amplitude of the power spectra). Right of the annulus is a color-bar corresponding to the temperature field (right scale) and the logarithm of the amplitude of the thermal power (left scale).

number is increased (due to the reduced lateral dimensions of downwelling conduits). Mobility is greater for higher nondimensional yield stresses as Ra_T is increased, consistent with a greater effective Rayleigh number producing the higher nondimensional stresses necessary to both rupture and drive the motion of the surface. (It should be noted that increases in Ra_T do not necessarily result in an increase in the dimensional yield stress, e.g., Foley & Becker 2009; van Heck & Tackley, 2011.) However, overall, significant changes in plateness and mobility are not observed for the factor of five increase in Ra_T investigated. In contrast, as is the case for isoviscous convection (Deschamps et al., 2010; Shahnas et al., 2008; Weller et al., 2016), for this Rayleigh number increase (with H fixed) the PCH increases significantly as Ra_T is increased (by approximately 25% for the cases with higher Ra_T) in accord with a drop in the mean temperature.

3.5. The Effect of a Thermal Viscosity Contrast Increase

Figure 12 shows a snapshot from Model H30Y2e6′(7) with $Ra_T = 10^9$, $d_f = 0.025$ and $\Delta\eta_T = 3.2 \times 10^6$, where the thermal viscosity contrast has been increased by an order of magnitude and Ra_T is 10^9. The nondimensional viscosity at the surface of the calculations is increased by increasing $\Delta\eta_T$ but decreased by increasing Ra_T in the absence of stress-dependent influences (i.e., if the change in Ra_T is taken as entirely due to changes in viscosity) so the nondimensional surface viscosity in this case is therefore effectively twice the value specified in the case depicted in Figure 4. The adjustment of the model parameters thus raises the Rayleigh number (by approximately a factor of 5) in the lowest region of the mantle, relative to cases in Figure 4, while lowering the local Rayleigh number at the surface (by approximately a factor of 2).

The net effect is that despite the increase in Ra_T, Ra_{eff} in Figure 12 is reduced in comparison to the case shown in the second plot of Figure 4. Nevertheless, increasing the thermal viscosity contrast results in reducing the generation of cold drips near the surface. The resulting warmer interior diminishes heat flow across the CMB (PCH drops from 17.3 to 14.9) and produces a spectrum with far less power in the larger frequencies. The time-averaged mobility of the surface remains almost unchanged relative to the calculation featuring a Ra_T and $\Delta\eta_T$ that are reduced by an order of magnitude (Model H30Y2e6(2)). However, the plateness experiences a mild increase (from 0.643 to 0.673). This finding is consistent with stiffening of the cold plate, reduced deformation induced by cold drips, and the resulting decrease in surface lateral velocity gradients. Increasing $\Delta\eta_T$ therefore increases plateness.

3.6. The Effect of the Surface Yield Stress

In all calculations described until now the cohesion, μ, has been set to a surface value of zero. Accordingly, increasing yield stress was accomplished by increasing $\sigma_{ductile}$ and therefore, simultaneously, the gradient of the yield stress increase throughout the region of depth d_f (see Figure 1). However, this choice also implies the surface (i.e., top boundary) will yield in response to any stress. Here we consider the effect of increasing the surface value systematically, up to a magnitude equal to $\sigma_{ductile} = 10^7$.

In order to continue to obtain the thinner upper thermal boundary layers obtained for calculations described in the previous two sections, we again specify $Ra_T = 10^9$. With this Rayleigh number, the calculations described feature internal Rayleigh numbers of roughly 3–17 $\times 10^5$. The variable yield stress region has a thickness of 2.5% ($d_f = 0.025$). A summary of these calculations can be found in the supporting information Table S8.

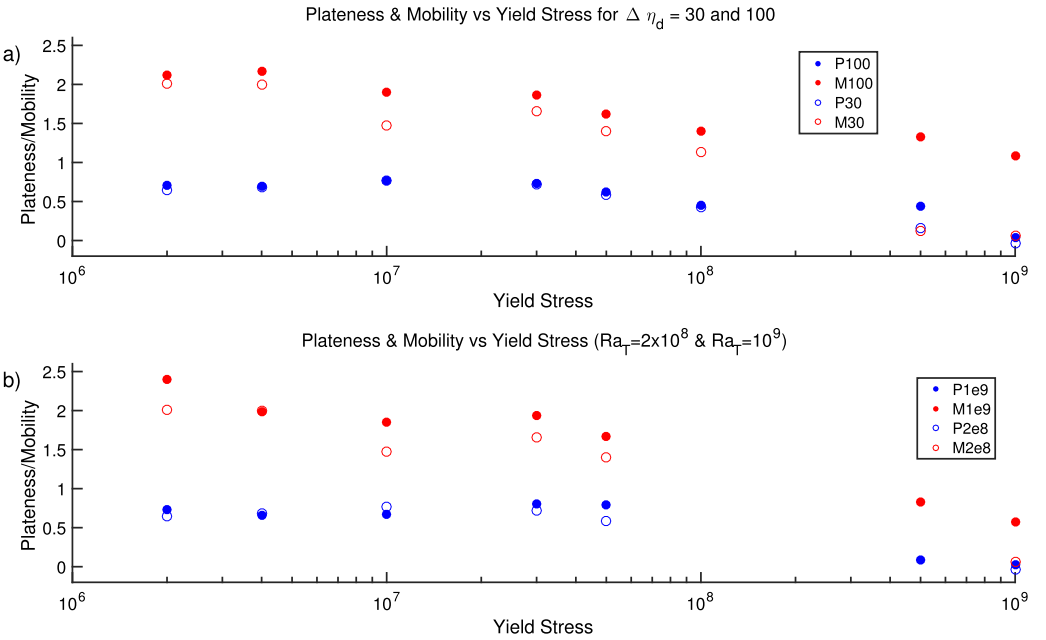

Figure 11. (a) Plateness (blue) and mobility (red) plotted against yield stress ($\sigma_{ductile}$) for cases with a lower mantle viscosity increase of 100 (filled circles) and 30 (empty circles). In all cases $\Delta\eta_T = 3.2\times10^5$ and $\mu = 0$. $Ra_T = 2\times10^8$ and 5×10^8 for calculations with lower mantle viscosity increases of 30 and 100, respectively. (b) Plateness (blue) and mobility (red) plotted against yield stress ($\sigma_{ductile}$) for cases with Rayleigh numbers of 10^9 (filled circles) and 2×10^8 (empty circles). $d_f = 0.05$ and 0.025, respectively. In all cases $\Delta\eta_T = 3.2\times10^5$, H = 30, and $\mu = 0$.

In Figure 13, cohesion is varied from zero to 1×10^7. so that surface failure decreases and the mean temperature increases. Temperature field power spectra show a dramatic decrease in shallow and midmantle amplitudes at frequencies greater than two as μ approaches $\sigma_{ductile}$. In addition, a subadiabatic gradient develops between the thermal boundary layers as heat builds in the upper mantle below the strong plates. As yield stress is increased either by increasing μ or $\sigma_{ductile}$ (Figure 4), a smaller number of downwellings become more focused and penetrate to the CMB. Although the mantle temperature is warmer as cohesion is increased, a similar amount of cold material is apparently delivered to the deep mantle by the small number of focused downwellings so that PCH is not affected substantially. However, the plateness increases dramatically as, by raising the strain rate threshold required for yielding, the increase in μ suppresses the formation of weakness associated with smaller instabilities at the surface.

The effect of increasing thermal viscosity contrast by an order of magnitude is presented in Figure 14 for an analogous sequence of models to those shown in Figure 13. Increasing $\Delta\eta_T$ by an order of magnitude while holding Ra_T fixed decreases the effective Rayleigh number by raising the nondimensional viscosity values everywhere above the CMB. The net effect of changing the thermal viscosity contrast is an increase in plateness and decrease in PCH. The first effect results from stiffening of the plates and a reduction in plate interior velocity gradients and the latter effect follows the lowering of the effective Rayleigh number.

A comparison of the plateness and mobility for the calculations shown in Figures 13 and 14 is presented in Figure 15a. An increase in plateness is seen when increasing cohesion while mobility and PCH (Figure 15b) exhibit less clear trends. However, both PCH and the heat flux from the core, q_{core} (Figure 15c) increase modestly with the increase in plateness. This appears to be explained by the focusing of downwellings with increased plateness and the deep penetration of the downwellings that envelop the CMB (see Figures 13 and 14). Accordingly, robust plateness appears to bolster the dynamo requirement of substantial heat flow from the core.

As described in section 3.5, for a given cohesion, plateness is increased when $\Delta\eta_T$ is increased. The variation in mobility, particularly fluctuations as yield stress is increased in the case where $\Delta\eta_T = 3.2\times10^6$, could possibly be due to the time-average of the number of convection cells changing in different cases, but this has not been verified. The increase in plateness with μ occurs for both of the thermal viscosity contrasts

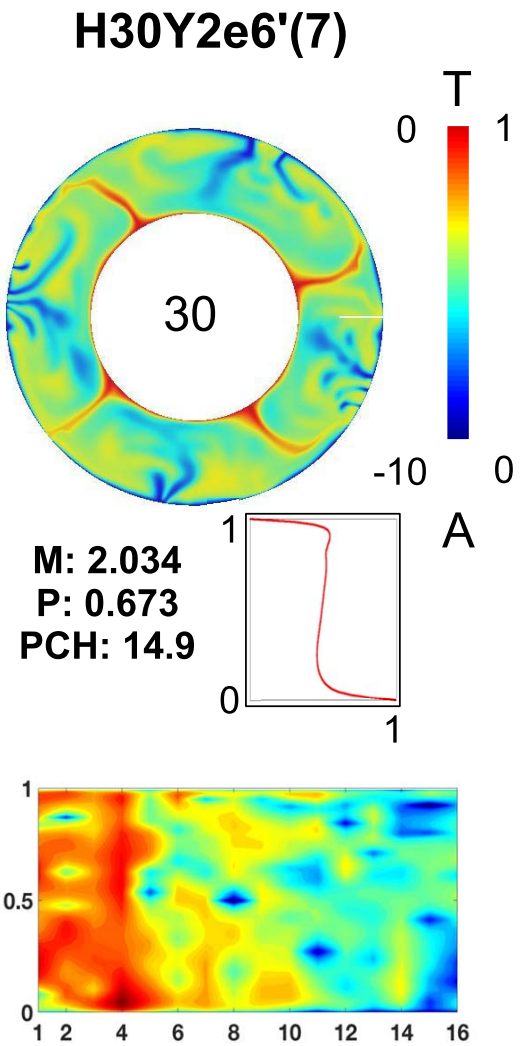

Figure 12. A case similar to that in the second plot of Figure 4 (Model H30Y2e6(2)) but with an increased thermal viscosity contrast and Ra_T. The radially averaged temperature profile (plotted as altitude versus temperature) and logarithm of the temperature power spectra (plotted as altitude versus amplitude of the power spectra) are also plotted. The color-bar scale indicates the magnitude of the temperature field values (right) and logarithms of the amplitude of power (left).

specified and is consistent with a diminished number of locations that feature yielding when μ is increased. Models featuring a thermal viscosity contrast of 3.2×10^6 also exhibit a general increase in mobility with cohesion. Maximum plateness of 0.915 is obtained with a uniform mantle yield stress (Model H30Y1e7′(8) with $\mu=1\times10^7$, $Ra_T=1\times10^9$, $d_f=0.025$, and $\Delta\eta_T=3.2\times10^6$)

3.7. Time-Dependence

Given the number of calculations presented in this study, it is not possible to examine the time-dependent behavior exhibited by each case. In this section, we describe the time-dependence of the model featuring the highest plateness in Figure 14. Typical evolution of Model H30Y1e7′(8), with $\mu=1\times10^7$, $Ra_T=10^9$, $d_f=0.025$, and $\Delta\eta_T=3.2\times10^6$ is presented in Figure 16. Multiple snapshots of the temperature field are shown at intervals indicated in terms of "transit time," t, which is defined by the thickness of the modeled mantle, d, over the temporal average of the spatial root-mean-square of the velocity field, V_{RMS}. (One transit time is therefore the time required to traverse the mantle at velocity V_{RMS}.) The $t=0$ snapshot for the sequence is the final plot from Figure 14.

The snapshots in Figure 16a show that the downwellings that develop in Model H30Y1e7′(8), with $\mu=1\times10^7$, $Ra_T=10^9$, $d_f=0.025$, and $\Delta\eta_T=3.2\times10^6$ range from short-lived transient features that form and then detach from the surface thermal boundary layer as their deepest points reach the base of the mantle (e.g., at one o'clock from 1.375t to 1.625t) to longer enduring downwellings that continue to draw cold material from the upper thermal boundary layer over sustained periods (e.g., between 10 and 11 o'clock prior to 0.0t to beyond 1.25t). In terrestrial terms, model slabs thus frequently reach lengths in excess of the mantle depth. The time series presented in Figure 16b show that the plateness remains strong and steady throughout the period modeled (consistent with the low variances indicated in Figure 8) while mobility varies much more and with greater frequency. (The fluctuations in mobility are consistent with the frequent formation and detachment of the most transient downwellings.) The variations in mobility result in maximum surface heat flux values that exceed minimum values by nearly 80% (Figure 16c) so that, because the internal heating rate is constant, the calculated value of the percentage of the heat flow coming from the core also varies greatly (from 18% to 30%). Alternatively, because the instantaneous PCH $\times q_{surf}=f^2 q_{core}$, maximum PCH should exceed minimum by nearly 80% if q_{core} is approximately constant. In fact, the blue curve in Figure 16c shows maximum core heat flux that exceeds minimum values by approximately 20%. Nevertheless, PCH does vary by roughly 80% and most of the actual variation in the calculated PCH result from fluctuations in surface velocity.

3.8. Thermochemical Convection

To determine the impact of proposed compositional provinces in the lower mantle on both core heat loss and the modeling of plates, we conclude by considering four cases that feature the emplacement of an initial uniform thickness compositionally anomalous intrinsically dense (CAID) layer enveloping the CMB. The initial temperature field prescribed for these calculations is from Model H30Y1e7′(8) shown in the last plot of Figure 14 and all parameters in the thermochemical calculations are identical to those of that model, with the exception of the introduction of the compositional component. Once the layer is introduced all cases are integrated forward in time until no long-term heating or cooling trends exist. Following convergence on a statistically steady state we continue to integrate and start the calculation of mean values for M,

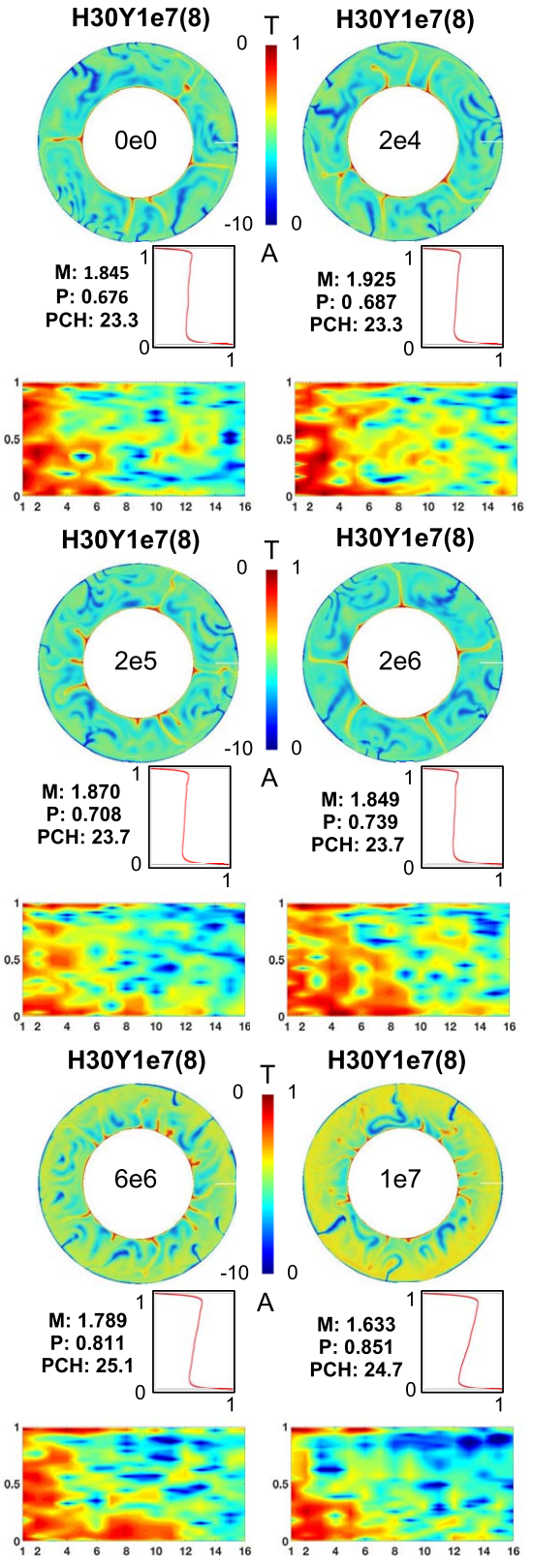

Figure 13. (continued)

P, PCH, and Ra_{eff}. Findings from these calculations are summarized in the supporting information Table S4 which also gives the buoyancy ratio for the CAID material and its volume as a percentage of the associated spherical shell.

In Figure 17, we show snapshots of the temperature field (a) and corresponding composition field (b) from one of the cases reported in the supporting information Table S4. This calculation features a buoyancy ratio of 0.7 and the dense material occupies 3.5% of the associated spherical shell. The CAID material has aggregated into two dominant provinces that occasionally migrate in response to relocation of the downwellings. The introduction of the CAID material actually produces a mild increase in the temporal average of the plateness, relative to the case where it is absent, with no clear dependence of plateness on buoyancy ratio for the two cases that we examined. We also found plateness to be insensitive to the two volumes of CAID material that we tested (3.5% versus 5%), however, we did find that mobility was slightly diminished by increasing the volume of the intrinsically dense component. We speculate that the effect of the CAID material on plateness could be a result of its effect on upwelling buoyancy. Upwellings are frequently present at the edges of the dense provinces and may therefore be slightly less buoyant in cases where CAID material is present. A reduction in the rate of evolution of the convection pattern (i.e., planform in three dimensions) permitted by reduced upwelling mobility may reduce the frequency with which new weak zones in the lithosphere can appear, thus bolstering the plateness statistic.

The trapping of heat in the deep dense provinces affects the lateral average of the temperature in the deepest part of the mantle where the thermal gradient at the CMB is reduced (Figure 17c). However, the mean temperature as a function of depth retains a subadiabatic gradient between the thermal boundary layers. Figure 17d shows that the power spectra of the temperature field is dominated by higher amplitudes in the lowest five frequencies, with some additional power peaking in the 12th degree due to a combination of internal convection in the interiors of the CAID provinces and several upwellings that are breaking away from the CMB outside the CAID provinces. Power remains strongest at degree two in the midmantle and upper mantle but is not as great as in the deep mantle.

The most significant impact of the CAID material is on heat loss from the core. Both an increase in the volume of the material and the buoyancy ratio act to diminish core heat flow by increasing the area of the

Figure 13. Cohesion, μ, is varied from 0 to 10^7 for cases featuring a depth-dependent increase in yield stress for the upper 2.5% of the mantle's depth ($d_f = 0.025$) and a fixed yield stress of $\sigma_{ductile} = 1 \times 10^7$ for the lower 97.5% of the mantle. Cohesion values are placed in the center of each corresponding annulus. A thermal viscosity contrast of $\Delta\eta_T = 3.2 \times 10^5$ is specified in all calculations and $Ra_T = 1 \times 10^9$ in all models. Values of temporally averaged mobility, M, plateness, P, and percent-core-heating, PCH, are given for each case below the temperature field snapshots. Temperature field power spectra (plotted as altitude versus power) and profiles of the laterally averaged temperatures (plotted as altitude versus temperature) are also presented. Color-bars correspond to both the nondimensional temperature (right scale) and the amplitude of the logarithm of the power spectra (left scale) of the thermal field.

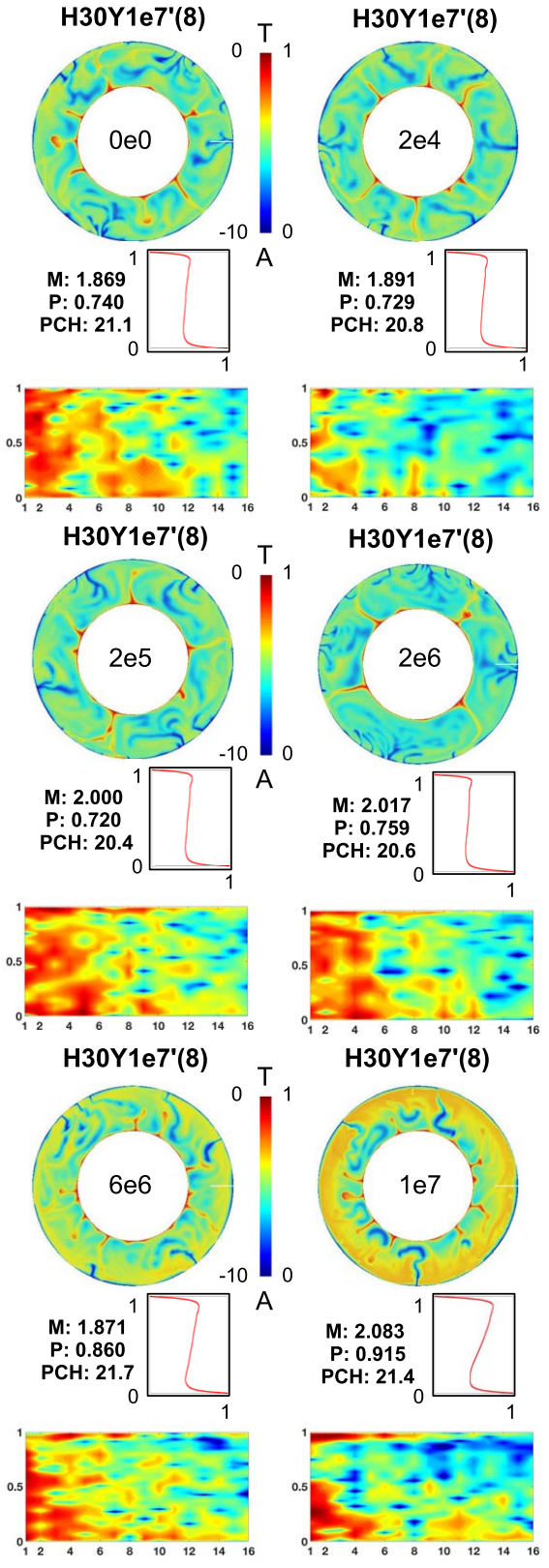

Figure 14. As in Figure 13 but for cases with a thermal viscosity contrast of $\Delta\eta_T = 3.2\times10^6$. Model details are given in the supporting information Table S8. Model identifiers are denoted with a prime to indicate a change in $\Delta\eta_T$ (as in the supporting information Table S8).

CMB that is covered by the insulating provinces. The cases with a buoyancy ratio of 1.0 experience the greatest drop in heat loss from the core (supporting information Table S4). Figure 17e plots time series of the PCH from the cases summarized in the supporting information Table S4. The temporal average of the PCH drops from 21.5 in the case where CAID material is absent (magenta curve) to 9.1 in model Thermo_B1.0_V5.0 (the case with the densest and greatest volume of CAID material). Intermediate values of PCH are found by lowering either the buoyancy ratio or volume of the provinces. In the absence of a CAID component, the PCH varies by approximately 15% around its mean. However, the magnitude of temporal variations in PCH particularly increase when the buoyancy ratio of the dense component is increased (i.e., the blue and cyan curves vary from minimum to maximum by more than 100%). This finding is explained by the propensity of a CAID component layer of buoyancy ratio 1.0 to envelop the core (substantially dropping the PCH). However, intermittent sweeping of the relatively thin uniform layer into piles by viscous entrainment associated with the arrival of downwellings is not uncommon. Regions of the CMB where the CAID layer is swept aside produce high gradients in temperature that release pulses of heat from the hot core.

4. Discussion

In this study, we have aimed to find values for the various parameters that give a plate-like surface velocity field while allowing for a contribution to surface heat flux from the core in the range supported by current research on the thermal state of the modern-day Earth. To this end, we employ both the mobility and plateness metrics to quantify the quality of plate-like surface motion and the temporal average of PCH as well as q_{core} in order to identify models that might support a core dynamo. In general we have found that surface mobility of greater than 1.0 (Figure 7) is typical in the majority of the cases that exhibit both strong surface mobility and plate-like surface velocity fields. Moreover, our definition of P yields a value of 1.0 for perfect plateness. Accordingly, the product of plateness and mobility will be greater than 1.0 for systems in which plate-like surface motion is present (although other combinations of these parameters that yield such a product are clearly possible for cases with decidedly poor plateness).

In Figure 18, we attempt to identify values for the parameters that most successfully satisfy the requirements of plateness and relevant CMB heat flow by plotting the product of plateness and mobility against PCH (Figure 18a) and total nondimensional core heat flux (Figure 18b). The colors of each data point are indicative of the ductile yield stress specified in the case represented. The shape of the data points indicate the value (or a range of values) for H. Only cases where $\eta_D = 30$ are plotted and color data points all have a cohesion of zero. Solid symbols correspond to $Ra_T = 2\times10^8$ and open symbols correspond to $Ra_T = 10^9$. The black and white symbols in the insets have variable cohesion and a center dot indicates a greater value of η_T but also lower effective Rayleigh number. The vertical dashed lines in the figures have a value of 1.0. Somewhat strikingly, no cases with a yield stress greater than 3×10^7 produce a P × M value below 1.0. In gen-

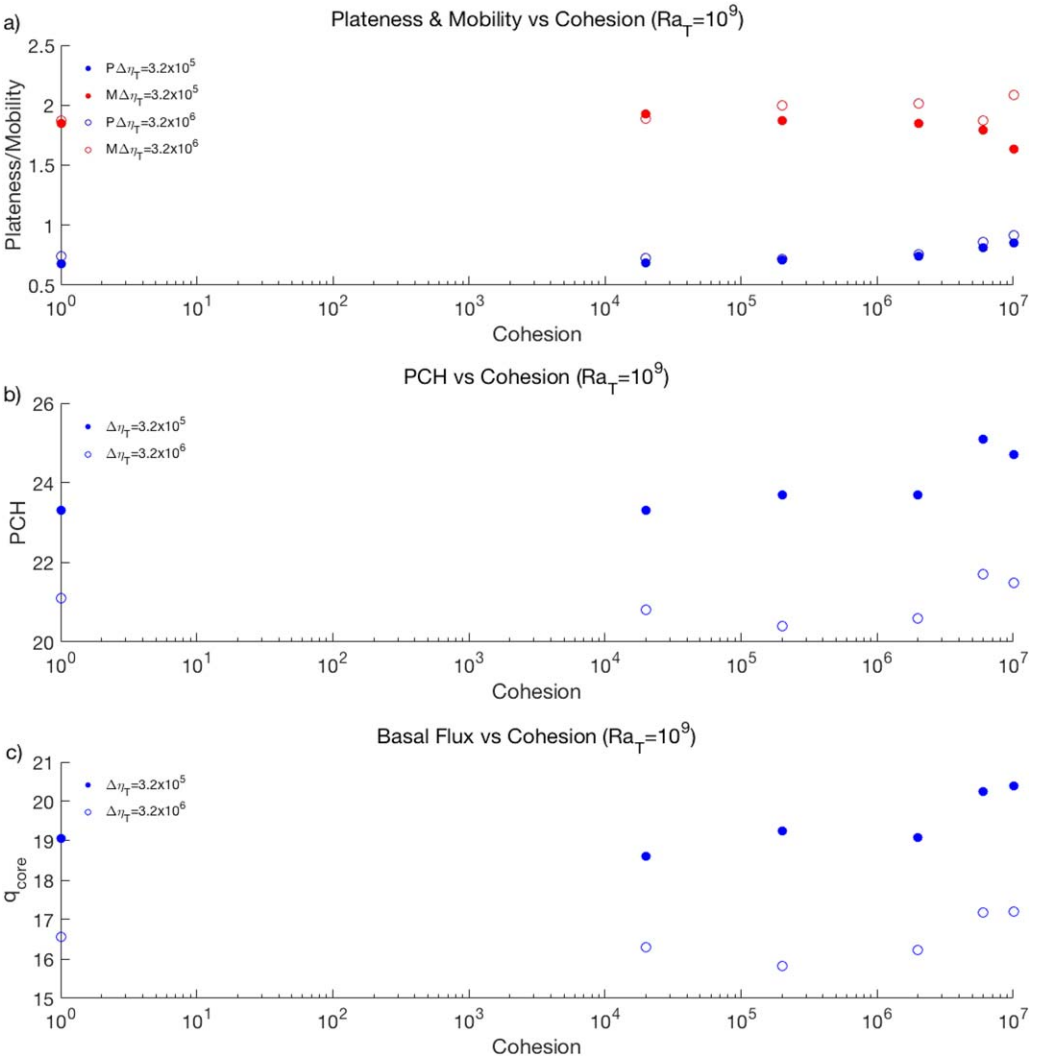

Figure 15. (a) Plateness (blue) and mobility (red) are plotted against cohesion (μ) for cases with a thermal viscosity contrasts of $\Delta\eta_T = 3.2\times10^5$ (filled circles) and $\Delta\eta_T = 3.2\times10^6$ (empty circles). (b) Percentage core heating (PCH) is plotted against cohesion (μ) for viscosity contrasts of $\Delta\eta_T = 3.2\times10^5$ (filled circles) and $\Delta\eta_T = 3.2\times10^6$ (empty circles). (c) Nondimensional basal heat flux (q_{core}) is plotted against cohesion (μ) for viscosity contrasts of $\Delta\eta_T = 3.2\times10^5$ (filled circles) and $\Delta\eta_T = 3.2\times10^6$ (empty circles).

eral, orange and red symbols sit well to the left of the vertical line, indicating that a plate-like surface is lost as yield stress is increased beyond the range associated with cyan to green yield stresses (i.e., $\sigma_{ductile}$ values of 1–5 $\times10^7$). Higher internal heating rates can be compatible with metrics indicating plate-like behavior, but as discussed below, typically feature shorter-lived "subduction" events. We found that varying H with $\sigma_{ductile}$ set to 1×10^7 (various cyan symbols) and μ set to zero allows for a wide distribution of PCH values that can be increased by increasing the Rayleigh number (open cyan symbols). However, Figure 18b shows that in contrast to PCH, the range of core heat flux values changes less in response to changing H. Thus, the addition of internal sources strongly affects surface heat flux (by increasing it) but has a much weaker effect on core heat flux. Accordingly, core heat flux requirements are not highly sensitive to the internal heating rate for the range of parameters investigated.

Given model parameters that yielded strong surface mobility when H = 30, for the range of internal heating rates that we investigated (25–90) we did not find that increasing the nondimensional internal heating rate produced the onset of stagnant-lid convection. Instead, we find substantial time-dependence (i.e., the longevity of downwellings and associated weak zones diminishes) and, as expected, a drop in the PCH (Figure 9a).

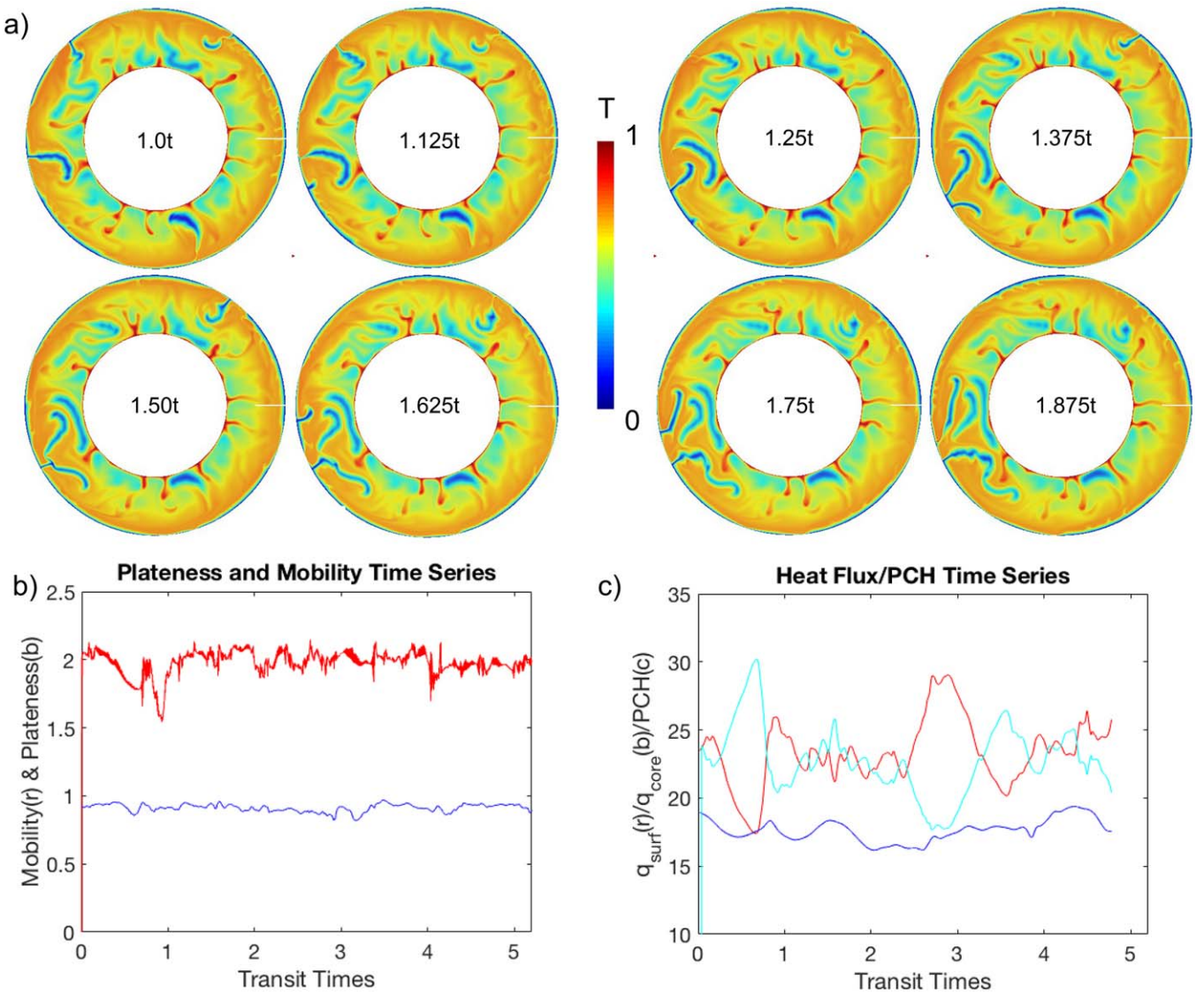

Figure 16. Time series of temperature field snapshots corresponding to Model H30Y1e7′(8), with $\mu=1\times10^7$, $Ra_T=1\times10^9$, $d_f=0.025$, and $\Delta\eta_T=3.2\times10^6$. (a) The snapshots correspond to different model times denoted by the value appearing within each annulus (given as a transit time, see text). Time series for plateness and mobility (b) as well as heat flux and PCH (c) are included below. Time 0.0t corresponds to the final plot of Figure 14. A color-bar corresponding to temperature magnitude is included. A single transit time is equal to 9.72×10^{-4} diffusion times and approximately 0.25 billion years.

For the cases in which we vary H plateness was found to be essentially independent of H while mobility showed no systematic trend (e.g., Figure 6c). Our findings are not necessarily contradictory of other studies but indicate that the transition to stagnant-lid with increasing H may be particularly sensitive to system geometry (Korenaga, 2009; O'Farrell et al., 2013) as well as yield stress. The geometrical effect is illustrated by considering that in the spherical geometry for calculations presented here the mean nondimensional temperature remains well below 1.0 even when H = 90, thus viscous coupling of the upper mantle to the lithosphere remains strong and a stagnant-lid is more difficult to obtain than in a Cartesian geometry (Yao et al., 2014). Moreover, the yield stresses implemented (e.g., blue to green symbols in Figure 18a) may be too far below the value necessary to transition to stagnant-lid convection regardless of the value of H. Similarly, for a yield stress above some critical value, a stagnant-lid will be obtained even when H = 0. Thus, for H to have a strong effect on mobility the system must be close to the episodic regime when H = 0 or higher.

The sequence of calculations that increase internal heating rate while holding all others parameters constant in value presents a rudimentary model of a cooling Earth when considered case by case from high H

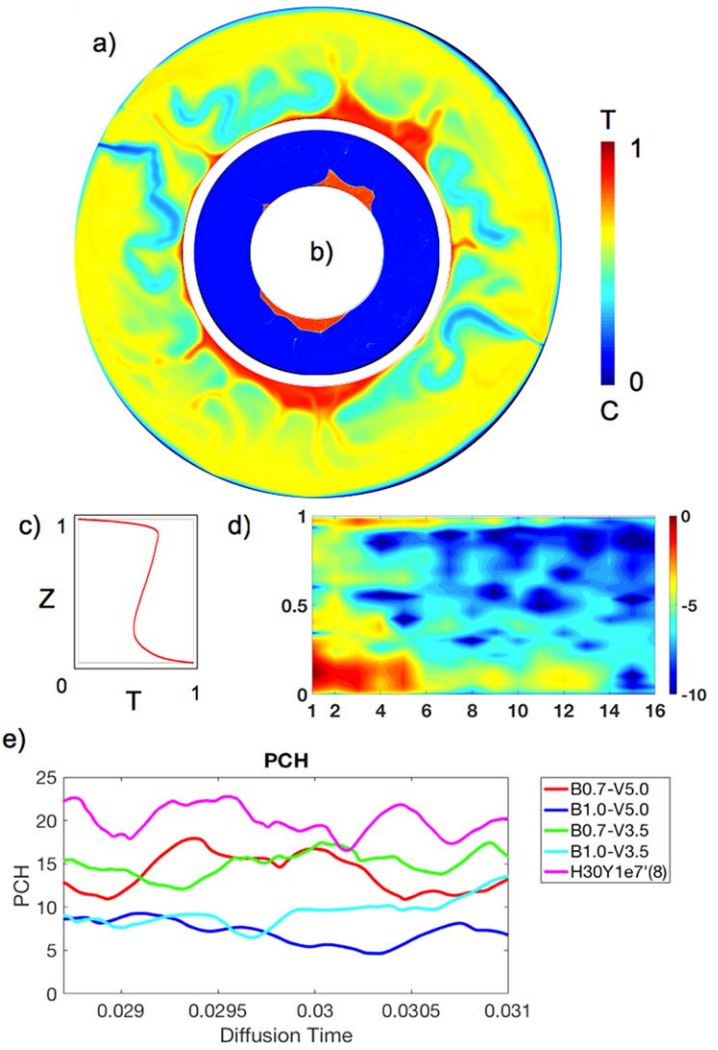

Figure 17. (a) Nondimensional temperature and (b) composition fields for Model Thermo_B0.7_V3.5. The color-bar scale for composition ranges from 0 (no enriched material present) to 1 (100% enriched material). The radially averaged temperature profile (c) is placed below the temperature field alongside the temperature spectra (d) corresponding to the thermal field appearing in Figure 17(a). (e) Time series of the percent-core-heating corresponding to calculations listed in supporting information Table S4 as well as Model H30Y1e7′(8), with $\mu=1\times10^7$, $Ra_T=1.\times10^9$, $d_f=0.025$, and $\Delta\eta_T=3.2\times10^6$. A diffusion time of 0.03 is approximately 8 billion years.

to low H values (see Figure 5). For example, considering the calculations where $\sigma_{ductile}=10^7$ this sequence shows that as the internal heating rate drops, there is relatively little impact on surface mobility or plateness. However, there is a monotonic increase in the PCH that occurs in tandem with cooling of the mantle. Although plateness and mobility are affected only weakly by the change in H (Figure 6c) in Figure 5 a clear change in the surface and interior dynamics is discernible as the convection increases in wavelength and the downwellings become longer-lived and more penetrative of the lower mantle (as H is reduced). This finding is consistent with previous work by van Hunen and van den Berg (2008) who concluded that ongoing subduction on the young Earth may have been obstructed by frequent slab detachment due to thermal weakness. However, we find that due to reinitiation of subduction, allowed by more common weak points elsewhere in the lithosphere, both mobility and good plateness may coexist with a hotter mantle.

Given that we do not model a time-dependent internal heating rate or cooling CMB, we do not explicitly model secular cooling of the mantle or core. However, the steady values of H that are specified in our calculations are not meant to reflect a current-day internal heating rate owing to radiogenic heating of the mantle. Rather, H represents heat available in the mantle from both current radioactivity and energy being lost through secular cooling. Accordingly, H does not represent any single energy source but rather, by its influence on mantle temperature, determines the fraction of heat loss from the surface that is derived from the core. An appropriate magnitude for H is thus a value which results in a core heat flux that accounts for a fraction of the surface flux within a desired range (i.e., PCH in a given range). A consequence of employing a steady value for H and the CMB temperature is that the "evolution" of these calculations (e.g., as shown in Figure 16) does not model realistic planetary evolution that should exhibit a cooling trend (or a heating trend in a situation such as evolution following the cessation of surface motion). Instead, the evolution we model emulates a nonageing (quasi steady temperature) planet. As in other mantle convection studies, a number of other idealizations implemented in our calculations should also be noted. For example, although we have focused on the plateness parameter and the entailed plate-like qualities of different calculations, none of the cases presented features the one-sided mode of subduction that characterizes mantle convection on Earth.

Using approximations of the mean global values of the parameters that comprise the Rayleigh number, and arguments that the upper thermal boundary layer for whole mantle convection should be comparable to oceanic slab thickness, isoviscous models of whole mantle convection have established an estimate for the mantle's Rayleigh number in the range 6×10^6 to 10^7 (e.g., Jarvis & Peltier, 1982). In Figure 19, we plot the magnitude of the internal Rayleigh number, from calculations listed in the supporting information Tables S2 and S3, against internal heating and the yield stress $\sigma_{ductile}$. For cases exhibiting plate-like surface behavior and PCH between 5% and 25%, $\sigma_{ductile}$ is 2×10^6 to 2×10^7 with H = 25–30. With these parameters we find Ra_{int} values between 3×10^5 and 10^6. However, as noted in section 2.4, Ra_{int} for the rheologically complex models can be more than an order of magnitude less than Ra based on boundary layer scaling from isoviscous models yielding the same vigor (see supporting information Table S5). Thus, with $Ra_T=2\times10^8$ we find a convective vigor in the plate-like regime that is too low for terrestrial whole mantle convection, but not by more than one order of magnitude. (One manifestation of lower Rayleigh number in the system interior is the magnitude of the subadiabatic gradients in the radial temperature profiles of many models (Sinha & Butler, 2007).) Increasing

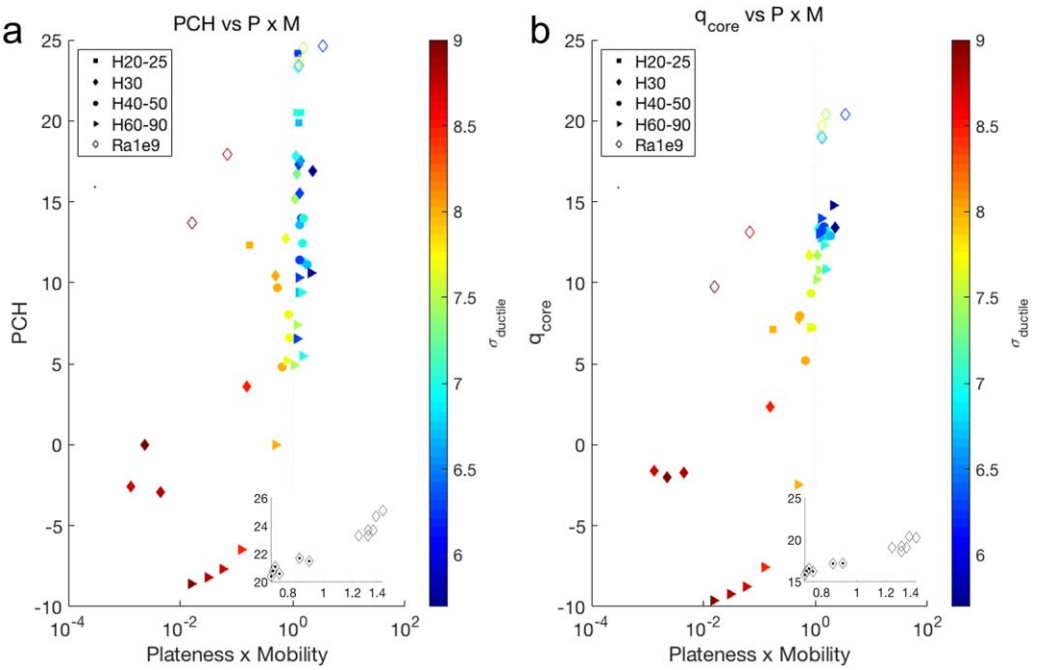

Figure 18. The product of plateness and mobility plotted against (a) the percentage of core heating (PCH) and (b) the core heat flux (q_{core}) for models from the supporting information Tables S2 and S3 (squares, diamonds, circles, triangles), ?? (black open diamonds), and ?? (black open diamonds with center dot). Data-point colors indicate the logarithm of ductile yield stress indicated by the color-bar (and all such cases feature $\mu = 0$). Black open diamonds (with and without center dot) have a ductile yield stress of 10^7 in all cases and variable cohesion.

H pushes the internal Rayleigh number closer to the terrestrial value but at the expense of not maintaining PCH in the range inferred for the current-day Earth. Moreover, as described above, downwellings become more dispersed but more transient. Similarly, increasing the yield stress pushes the internal Rayleigh number closer to the terrestrial magnitude but the convective regime becomes episodic. In contrast, relaxing the yield stress causes the internal Rayleigh number to drop to values of roughly 10^5 due to the increase in thermally dependent viscosity with increased cooling that accompanies the mobile surface. To summarize, a posteriori Rayleigh numbers (Ra_{eff} and Ra_{int}) determined for the cases in the supporting information Table S2, featuring the strongest plateness and a PCH that may be Earth-like, are perhaps an order of magnitude less than the effective Rayleigh number estimates for the current-day Earth. Calculations presented in the supporting information Tables S4, S7, and S8 are close to the convective vigor estimates for the current-day Earth.

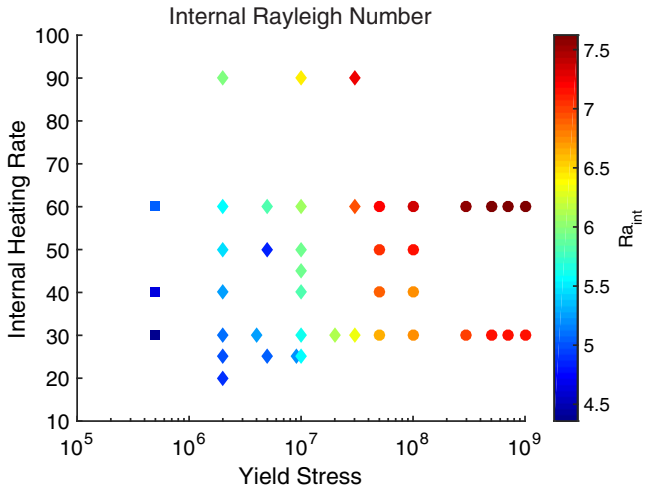

Figure 19. A regime plot analogous to Figure 9 (a) and (b) with internal heating rate, H, plotted against yield stress ($\sigma_{ductile}$). Data-point colors indicate the logarithm of internal Rayleigh number Ra_{int} indicated by the color-bar. Squares, diamonds and circles indicate the mobile, plate-like and transitional/sluggish-lid regimes, respectively.

A notable difference of our findings from previous studies (Foley & Becker, 2009) is that we find plate-like surface motion (specifically plateness) is improved by increasing the near surface yield stress (i.e., throughout the region of thickness d_f). With low surface yield stress, μ, we find that weakness in the upper thermal boundary layer occurs with enough frequency that zones of high deformation are commonplace. Given a value of $\sigma_{ductile}$ that results in convection characteristic of the nonplate-like mobile regime when $\mu = 0$, increasing μ was found to focus zones of weakness in the upper thermal boundary layer without adversely affecting mobility so that maximum plateness occurs when $\sigma_{ductile} = \mu$. The apparent contradiction of this finding with behavior reported previously (Foley & Becker, 2009; van Heck & Tackley, 2008) is explained by the starting value of $\sigma_{ductile}$. In practice, once $\sigma_{ductile}$ reaches a specific threshold

value, stress induced reductions of the viscosity at depths greater than d_f will never occur. For much higher $\sigma_{ductile}$ values, μ needs to be decreased to reach stress values where yielding of the surface can appear. For lower $\sigma_{ductile}$ values, surface yielding is attainable with $\mu=\sigma_{ductile}$ and decreasing μ further permits weakening of the surface in so many locations that strong plateness is lost. Stated alternatively, provided $\sigma_{ductile}$ is sufficiently high to suppress any yielding below a depth d_f, convective regime is determined entirely by yield stress magnitude in the layer associated with brittle failure not the relative values of μ and $\sigma_{ductile}$.

5. Conclusions

Multiple parameters enhance plate-tectonic-like characteristics in mantle convection models. However, plate-like surface motion does not ensure an interior thermal structure that is a reasonable emulation of terrestrial conditions. For example, convection may be obtained with an interior that is too hot (approaching or exceeding the solidus) or too cold (resulting in core heat flow in disagreement with the currently estimated range). The variation of mantle yield stress (μ, $\sigma_{ductile}$, d_f) and thermal viscosity contrast ($\Delta\eta_T$) has the strongest impact on a surface exhibiting plate-like features. We find that while having a minimal effect on the localization of deformation, increases in internal heating rate do have a significant influence on the temperature of the mantle and thus act to mitigate the PCH. Conversely, within the plate-like regime variations in yield stress allowed for a contrasting effect, such that increases to σ_{yield} allowed for improved plateness while having a small impact on core heat flux. Substantial variations in yield stress result in the widely described regime shift from that of a mobile/plate-like surface to that of an episodic and eventually stagnant-lid regime. Regime specific behavior is most notable in the time-dependence of mobility, for which the plate-like regime experiences relatively little variance (Figure 7) while both nonplate-like mobile and episodic regimes exhibit much more time-dependent behavior.

In addition to internal heating rate and ductile yield stress, several other parameters act to enhance or alter the plate-tectonic characteristics of the mantle along with the PCH. The influence of viscosity structure is directly explored through both increases in lower mantle viscosity and thermal viscosity contrast. An increase in lower mantle viscosity (from a factor of 30–100 relative to the upper mantle) yields short wavelength convection in the upper mantle, and some degree of layering (see Figure 10). However, this increase produces minimal effects on time-averaged plateness and mobility. Conversely, an increase in thermal viscosity contrast reduces the number of cold drips near the surface, effectively warming the interior and reducing the PCH. Increasing thermal viscosity contrast also stiffens the cold plates of the surface, reducing deformation near the surface and increasing the plateness. Thermal Rayleigh number is increased to investigate the influence of convective vigor on surface structure. Noteworthy increases in plateness and mobility are not observed, however, PCH is affected significantly. The rheological structure of the mantle is further investigated through the systematic increase of surface yield stress (cohesion). Increases in cohesion precipitate a reduction in the number of downwellings leading to an increased mean temperature and the development of a subadiabatic gradient between the thermal boundary layers. Despite a warmer interior, PCH is not considerably affected. However, plateness increases markedly, yielding a "best case" value of 0.915, a value that is increased even further in models possessing compositionally anomalous intrinsically dense (CAID) material near the CMB.

The introduction of CAID material mildly increases the temporally averaged plateness, but showed no clear dependence on buoyancy ratio for the four cases investigated. Additionally, for the volumes we tested, plateness is found to be insensitive to the volume of CAID material while mobility decreases slightly when CAID volume is increased. CAID material was found to coalesce into two distinct provinces for periods of time ranging from 75 to 200 Myr, so that it has a significant influence on core heat flow where both the volume and buoyancy ratio act to diminish heat loss from the core. An increased volume and buoyancy ratio lead to an insulation of regions of the CMB, trapping heat in the core. An increase in these parameters also leads to a greater time-dependence in PCH. In summary, for the cases examined we do not find the presence of a CAID mantle component adversely affects the formation of plates. However, it may strongly influence core heat loss. Future studies should further explore the influence of compositional heterogeneity in the mantle on both the evolution of surface mobility and core heat loss.

Acknowledgments
We thank Matt Weller and two anonymous reviewers for very constructive feedback on this manuscript. S.M.L. and J.P.L. are grateful for funding from the NSERC of Canada (fund: 327084-10). Representative output data from all calculations analyzed in this study appear in the tables found in the supporting information. Further detail is available by contacting the corresponding author. Calculations were performed on the GPC cluster at the SciNet GPC Consortium and on the Saw and Orca clusters at the Sharcnet Consortium. SciNet is funded by the Canada Foundation for Innovation under the auspices of Compute Canada; the Government of Ontario; Ontario Research Fund—Research Excellence; and the University of Toronto. This work was also made possible by the facilities of the Shared Hierarchical Academic Research Computing Network (SHARCNET: www.sharcnet.ca) and Compute/Calcul Canada.

References

Bercovici, D. (2003). The generation of plate tectonics from mantle convection. *Earth and Planetary Science Letters*, *205*(3–4), 107–121. https://doi.org/10.1016/S0012-821X(02)01009-9

Bercovici, D., Schubert, G., & Glatzmaier, G. (1989). Three-dimensional spherical models of convection in the Earth's mantle. *Science*, *244*(4907), 950–955.

Boehler, R. (2000). High pressure experiments and the phase diagram of lower mantle and core materials. *Reviews of Geophysics*, *38*(2), 221–245.

Buffett, B. A. (2003). The thermal state of Earth's core. *Science*, *299*(5613), 1675–1677.

Buffett, B. A. (2007). Taking earth's temperature. *Science*, *315*(5820), 1801–1802.

Buffett, B. A. (2002). Estimates of heat flow in the deep mantle based on the power requirements for the geodynamo. *Geophysical Research Letters*, *29*(12), 1566. https://doi.org/10.1029/2001GL014649

Bunge, H. P. (2005). Low plume excess temperature and high core heat flux inferred from non-adiabatic geotherms in internally heated mantle circulation models. *Physics of the Earth and Planetary Interiors*, *153*(1–3), 3–10.

Christensen, U. R. (1984). Heat transport by variable viscosity convection and implications for the Earth's thermal evolution. *Physics of the Earth and Planetary Interiors*, *35*(4), 264–282.

Christensen, U. R., & Tilgner, A. (2004). Power requirement of the geodynamo from ohmic losses in numerical and laboratory dynamos. *Nature*, *429*(6988), 169–171.

Coltice, N., Gerault, M., & Ulvrova, M. (2017). A mantle convection perspective on global tectonics. *Earth Science Reviews*, *165*, 120–150.

Combes, M., Grigne, C., Husson, L., Conrad, C. P., Le Yaouanq, S., Parenthoen, M., et al. (2012). Multiagent simulation of evolutive plate tectonics applied to the thermal evolution of the Earth. *Geochemistry, Geophysics, Geosystems*, *13*, Q05006. https://doi.org/10.1029/2011GC004014

Davies, G. F. (1988). Ocean bathymetry and mantle convection. 1: Large-scale flow and hotspots. *Journal of Geophysical Research*, *93*(B9), 10467–10480. https://doi.org/10.1029/JB093iB09p10467

Davies, J. H., & Davies, D. R. (2010). Earth's surface heat flux. *Solid Earth*, *1*(1), 5–24.

Deschamps, F., Tackley, P. J., & Nakagawa, T. (2010). Temperature and heat flux scalings for isoviscous thermal convection in spherical geometry. *Geophysical Journal International*, *182*, 137–154. https://doi.org/10.1111/j.1365-246X.2010.04637.x

Foley, B. J., & Becker, T. W. (2009). Generation of plate-like behavior and mantle heterogeneity from a spherical, viscoplastic convection model. *Geochemistry, Geophysics, Geosystems*, *10*, Q08001. https://doi.org/10.1029/2009GC002378

Gait, A. D., Lowman, J. P., & Gable, C. W. (2008). Time dependence in 3-D mantle convection models featuring evolving plates: Effect of lower mantle viscosity. *Journal of Geophysical Research*, *113*, B08409. https://doi.org/10.1029/2007JB005538

Gubbins, D., Alfe, D., Davies, C., & Pozzo, M. (2015). On core convection and the geodynamo: Effects of high electrical and thermal conductivity. *Physics of the Earth and Planetary Interiors*, *247*, 56–64. https://doi.org/10.1016/j.pepi.2015.04.002

Hager, B. H. (1984). Subducted slabs and the geoid: Constraints on mantle rheology and flow. *Journal of Geophysical Research*, *89*(B7), 6003–6015. https://doi.org/10.1029/JB089iB07p06003

Haskell, N. A. (1935). The motion of a viscous fluid under a surface load. *Journal of Applied Physics*, *6*(8), 265–269. https://doi.org/10.1063/1.1745329

Höink, T., & Lenardic, A. (2008). Three-dimensional mantle convection simulations with a low-viscosity asthenosphere and the relationship between heat flow and the horizontal length scale of convection. *Geophysical Research Letters*, *35*, L10304. https://doi.org/10.1029/2008GL033854

Höink, T., & Lenardic, A. (2010). Long wavelength convection, Poiseuille-Couette flow in the low-viscosity asthenosphere and the strength of plate margins. *Geophysical Journal International*, *180*(1), 23–33. https://doi.org/10.1111/j.1365-246X.2009.04404.x

Jarvis, G. T., & Peltier, W. R. (1982). Mantle convection as a boundary layer phenomenon. *Geophysical Journal International*, *68*(2), 389–427.

Jaupart, C., Labrosse, S., & Mareschal, J.-C. (2007). Temperatures, heat and energy in the mantle of the earth. *Treatise on Geophysics*, *7*, 253–303.

Kennett, B. L. N., & Bunge, H.-P. (2008). *Geophysical continua* (pp. 266–271). Cambridge, UK: Cambridge University Press.

King, S. D., & Masters, G. (1992). An inversion for radial viscosity structure using seismic tomography. *Geophysical Research Letters*, *19*(15), 1551–1554. https://doi.org/10.1029/92GL01700

Kohlstedt, D. L., Evans, B., & Mackwell, S. J. (1995). Strength of the lithosphere—Constraints imposed by laboratory experiments. *Journal of Geophysical Research*, *100*(B9), 17587–17602.

Korenaga, J. (2009). Scaling of stagnant-lid convection with Arrhenius rheology and the effects of mantle melting. *Geophysical Journal International*, *179*(1), 154–170. https://doi.org/10.1111/j.1365-246X.2009.04272.x

Korenaga, J. (2017). Pitfalls in modeling mantle convection with internal heat production. *Journal of Geophysical Research: Solid Earth*, *122*, 4064–4085. https://doi.org/10.1002/2016JB013850

Kuang, W. L., & Bloxham, J. (1997). An earth-like numerical dynamo model. *Nature*, *389*(6649), 371–374. https://doi.org/10.1038/38712

Labrosse, S. (2002). Hotspots, mantle plumes and core heat loss. *Earth and Planetary Science Letters*, *199*(1–2), 147–156. https://doi.org/10.1016/S0012-821X(02)00537-X

Labrosse, S. (2003). Thermal and magnetic evolution of the Earth's core. *Physics of the Earth and Planetary Interiors*, *140*(1–3), 127–143. https://doi.org/10.1016/j.pepi.2003.07.006

Labrosse, S. (2015). Thermal evolution of the core with a high thermal conductivity. *Physics of the Earth and Planetary Interiors*, *247*, 36–55. https://doi.org/10.1016/j.pepi.2015.02.002

Labrosse, S., Poirier, J. P., & Le Mouel, J. L. (1997). On cooling of the Earth's core. *Physics of the Earth and Planetary Interiors*, *99*(1–2), 1–17. https://doi.org/10.1016/S0031-9201(96)03207-4

Lambeck, K., Johnston, P., Smither, C., & Nakada, M. (1996). Glacial rebound of the British Isles—Iii: Constraints on mantle viscosity. *Geophysical Journal International*, *125*(2), 340–354. https://doi.org/10.1111/j.1365-246X.1996.tb00003.x

Lambeck, K., Smither, C., & Johnston, P. (1998). Sea-level change, glacial rebound and mantle viscosity for northern Europe. *Geophysical Journal International*, *134*(1), 102–144. https://doi.org/10.1046/j.1365-246x.1998.00541.x

Lay, T., Hernlund, J., & Buffett, B. A. (2008). Core-mantle boundary heat flow. *Nature Geoscience*, *1*(1), 25–32. https://doi.org/10.1038/ngeo.2007.44

Lay, T., Hernlund, J., Garnero, E. J., & Thorne, M. S. (2006). A post-perovskite lens and D″ heat flux beneath the central Pacific. *Science*, *314*(5803), 1272–1276. https://doi.org/10.1126/science.1133280

Lekic, V., Cottaar, S., Dziewonski, A., & Romanowicz, B. (2012). Cluster analysis of global lower mantle tomography: A new class of structure and implications for chemical heterogeneity. *Earth and Planetary Science Letters*, *357–358*, 68–77. https://doi.org/10.1016/j.epsl.2012.09.014

Lenardic, A., & Crowley, Jf. W. (2012). On the notion of well-defined tectonic regimes for terrestrial planets in this solar system and others. *The Astrophysics Journal*, *755*(2), 132.

Loddoch, A., Stein, C., & Hansen, U. (2006). Temporal variations in the convective style of planetary mantles. *Earth and Planetary Science Letters*, *251*(1–2), 79–89. https://doi.org/10.1016/j.epsl.2006.08.026

Mallard, C., Coltice, N., Seton, M., Muller, R. D., & Tackley, P. J. (2016). Subduction controls the distribution and fragmentation of Earth's tectonic plates. *Nature*, *535*(7610), 140–143. https://doi.org/10.1038/nature17992

Marquardt, H., & Miyagi, L. (2015). Slab stagnation in the shallow lower mantle linked to an increase in mantle viscosity. *Nature Geoscience*, *8*(4), 311–314. https://doi.org/10.1038/ngeo2393

Masters, G., Laske, G., Bolton, H., & Dziewonski, A. (2000). The relative behavior of shear velocity, bulk sound speed, and compressional velocity in the mantle: Implications for chemical and thermal structure, Earth's deep interior: In S. Karato et al. (Eds.), *Mineral physics and tomography from the atomic to the global scale* (pp. 63–87). Washington, DC: American Geophysical Union. https://doi.org/10.1029/GM117p0063

Mitrovica, J. X. (1996). Haskell [1935] revisited. *Journal of Geophysical Research*, *101*(B1), 555–569. https://doi.org/10.1029/95JB03208

Mitrovica, J. X., & Forte, A. M. (1997). Radial profile of mantle viscosity: Results from the joint inversion of convection and postglacial rebound observables. *Journal of Geophysical Research*, *102*(B2), 2751–2769. https://doi.org/10.1029/96JB03175

Mitrovica, J. X., & Forte, A. M. (2004). A new inference of mantle viscosity based upon joint inversion of convection and glacial isostatic adjustment data. *Earth and Planetary Science Letters*, *225*(1–2), 177–189. https://doi.org/10.1016/j.epsl.2004.06.005

Mitrovica, J. X., & Peltier, W. R. (1991). A complete formalism for the inversion of post-glacial rebound data: Resolving power analysis. *Geophysical Journal Intertional*, *104*(2), 267–288. https://doi.org/10.1111/j.1365-246X.1991.tb02511.x

Mittelstaedt, E., & Tackley, P. J. (2006). Plume heat flow is much less than CMB heat flow. *Earth and Planetary Science Letters*, *241*(1–2), 202–210.

Monnereau, M., & Quéré, S. (2001). Spherical shell models of mantle convection with tectonic plates. *Earth and Planetary Science Letters*, *184*(3–4), 575–587. https://doi.org/10.1016/S0012-821X(00)00334-4

Moresi, L., & Solomatov, V. (1995). Numerical investigation of 2D convection with extremely large viscosity variations. *Physics of Fluids*, *7*(9), 2154– 2162. https://doi.org/10.1063/1.868465

Moresi, L., & Solomatov, V. (1998). Mantle convection with a brittle lithosphere: Thoughts on the global tectonic style of the Earth and Venus. *Geophysical Journal International*, *133*(3), 669–682.

O'Farrell, K. A., Lowman, J. P., & Bunge, H.-P. (2013). Comparison of spherical-shell and plane-layer mantle convection thermal structure in viscously stratified models with mixed-mode heating: Implications for the incorporation of temperature-dependent parameters. *Geophysical Journal International*, *192*(2), 456–472. https://doi.org/10.1093/gji/ggs053

Pollack, H. N., & Chapman, D. S. (1977). Mantle heat flow. *Earth and Planetary Science Letters*, *34*(2), 174–184. https://doi.org/10.1016/0012-821X(77)90002-4

Pollack, H. N., & Chapman, D. S. (1977). On the regional variation of heat flow, geotherms, and lithospheric thickness. *Tectonophysics*, *38*(3–4), 279–296. https://doi.org/10.1016/0040-1951(77)90215-3

Pozzo, M., Davies, C., Gubbins, D., & Alfe, D. (2012). Thermal and electrical conductivity of iron at Earth/'s core conditions. *Nature*, *485*(7398), 355–358. https://doi.org/10.1038/nature11031

Ratcliff, J. T., Bercovici, D., Schubert, G., & Kroenke, L. W. (1998). Mantle plume heads and the initiation of plate tectonic reorganizations. *Earth and Planetary Science Letters*, *156*(3–4), 195–207. https://doi.org/10.1016/S0012-821X(98)00016-8

Richards, M. A., & Hager, B. H. (1984). Geoid anomalies in a dynamic Earth. *Journal of Geophysical Research*, *89*(B7), 5987–6002. https://doi.org/10.1029/JB089iB07p05987

Richards, M. A., Yang, W.-S., Baumgardner, J. R., & Bunge, H.-P. (2001). Role of a low-viscosity zone in stabilizing plate tectonics: Implications for comparative terrestrial planetology. *Geochemistry, Geophysics, Geosystems*, *2*(8), 1026. https://doi.org/10.1029/2000GC000115

Ritsema, J., Deuss, A. A., van Heijst, H. J., & Woodhouse, J. H. (2011). S40RTS: A degree-40 shear-velocity model for the mantle from new Rayleigh wave dispersion, teleseismic traveltime and normal-mode splitting function measurements. *Geophysical Journal International*, *184*(3), 1223–1236.

Rudnick, R. L., & Fountain, D. M. (1995). Nature and composition of the continental crust: A lower crustal perspective. *Reviews of Geophysics*, *33*(3), 267–309. https://doi.org/10.1029/95RG01302

Rudolph, M. L., Lekic, V., & Lithgow-Bertelloni, C. (2015). Viscosity jump in Earth's mid-mantle. *Science*, *350*(6266), 1349–1352.

Shahnas, M. H., Lowman, J. P., Jarvis, G. T., & Bunge, H.-P. (2008). Convection in a spherical shell heated by an isothermal core and internal sources: Implications for the thermal state of planetary mantles. *Physics of the Earth and Planetary Interiors*, *168*(1–2), 6–15. https://doi.org/10.1016/j.pepi.2008.04.007

Sigmundsson, F. (1991). Post-glacial rebound and asthenosphere viscosity in Iceland. *Geophysical Research Letters*, *18*(6), 1131–1134. https://doi.org/10.1029/91GL01342

Simmons, N. A., Forte, A. M., Boschi, L., & Grand, S. P. (2010). GyPSuM: A joint tomographic model of mantle density and seismic wave speeds. *Journal of Geophysical Research*, *115*, B12310. https://doi.org/10.1029/2010JB007631

Sinha, G., & Butler, S. L. (2007). On the origin and significance of subadiabatic temperature gradients in the mantle. *Journal of Geophysical Research: Solid Earth*, *112*, B10406. https://doi.org/10.1029/2006JB004850

Sleep, N. H. (1990). Hotspots and mantle plumes: Some phenomenology. *Journal of Geophysical Research*, *95*(B5), 6715–6736. https://doi.org/10.1029/JB095iB05p06715

Solomatov, V. S. (1995). Scaling of temperature and stress-dependent viscosity convection. *Physics of Fluids*, *7*(2), 266–274. https://doi.org/10.1063/1.868624

Stacey, F. D., & Davis, P. M. (2008). *Physics of the Earth*. New York, NY: Wiley.

Stein, C., Finnenkotter, A., Lowman, J. P., & Hansen, U. (2011). The pressure-weakening effect in super-Earths: Consequences of a decrease in lower mantle viscosity on surface dynamics. *Geophysical Research Letters*, *38*, L21201. https://doi.org/10.1029/2011GL049341

Stein, C., & Hansen, U. (2008). Plate motions and the viscosity structure of the mantle-Insights from numerical modelling. *Earth and Planetary Science Letters*, *272*(1–2), 29–40. https://doi.org/10.1016/j.epsl.2008.03.050

Stein, C., & Lowman, J. P. (2010). Response of mantle heat flux to plate evolution. *Geophysical Research Letters*, *37*, L24201. https://doi.org/10.1029/2010GL045283

Stein, C., Lowman, J. P., & Hansen, U. (2014). A comparison of mantle convection models featuring plates. *Geochemistry, Geophysics, Geosystems*, *15*, 2689–2698. https://doi.org/10.1002/2013GC005211

Stein, C., Schmalzl, J., & Hansen, U. (2004). The effect of rheological parameters on plate behavior in a self-consistent model of mantle convection. *Physics of the Earth and Planetary Interiors*, *142*(3–4), 225–255. https://doi.org/10.1016/j.pepi.2004.01.006

Tackley, P. J. (2000a). Self-consistent generation of tectonic plates in time-dependent, three-dimensional mantle convection simulations. *Geochemistry, Geophysics, Geosystems*, *1*(8), 1026. https://doi.org/10.1029/2000GC000043

Tackley, P. J. (2000b). The quest for self-consistent generation of plate tectonics in mantle convection models. In M. A. Richards, R. Gordon, & R. van der Hilst (Eds.), *The history and dynamics of global plate motions*. Washington, DC: American Geophysical Union. https://doi.org/10.1029/GM121p0047

Tackley, P. J., & King, S. D. (2003). Testing the tracer ratio method for modeling active compositional fields in mantle convection simulations. *Geochemistry, Geophysics, Geosystems*, *4*(4), 8302. https://doi.org/10.1029/2001GC000214

Trompert, R., & Hansen, U. (1998). Mantle convection simulations with rheologies that generate plate-like behavior. *Nature*, *395*(6703), 686–689.

Turcotte, D. L., & Schubert, G. (2014). *Geodynamics*. Cambridge, UK: Cambridge University Press.

van Heck, H. J., & Tackley, P. J. (2011). Plate tectonics on super-Earths: Equally or more likely than on Earth. *Earth and Planetary Science Letters*, *310*(3–4), 252–361. https://doi.org/10.1016/j.epsl.2011.07.029

van Heck, H. J., & Tackley, P. J. (2008). Planforms of self-consistently generated plates in 3D spherical geometry. *Geophysical Research Letters*, *35*, L19312. https://doi.org/10.1029/2008GL035190

van Hunen, J., & van den Berg, A. (2008). Plate tectonics on the early Earth: Limitations imposed by strength and buoyancy of subducted lithosphere. *Lithos*, *103*(1–2), 217–235. https://doi.org/10.1016/j.lithos.2007.09.016

Weller, M. B., & Lenardic, A. (2012). Hysteresis in mantle convection: Plate tectonics systems. *Geophysical Research Letters*, *39*, L10202. https://doi.org/10.1029/2012GL051232

Weller, M. B., & Lenardic, A. (2016). The energetics and convective vigor of mixed-mode heating: Velocity scalings and implications for the tectonics of exoplanets. *Geophysical Research Letters*, *43*, 9469–9474. https://doi.org/10.1002/2016GL069927

Weller, M. B., Lenardic, A., & Moore, W. B. (2016). Scaling relationships and physics for mixed heating convection in planetary interiors: Isoviscous spherical shells. *Journal of Geophysical Research: Solid Earth*, *121*, 7598–7617. https://doi.org/10.1002/2016JB013247

Yao, C., Deschamps, F., Lowman, J. P., Sanchez-Valle, C., & Tackley, P. J. (2014). Stagnant lid convection in bottom-heated thin 3-D spherical shells: Influence of curvature and implications for dwarf planets and icy moons. *Journal of Geophysical Research: Planets*, *119*, 1895–1913. https://doi.org/10.1002/2014JE004653

Yoshida, M. (2008). Mantle convection with longest-wavelength thermal heterogeneity in a 3-D spherical model: Degree one or two?. *Geophysical Research Letters*, *35*, L23302. https://doi.org/10.1029/2008GL036059

Zhong, S., & Watts, A. B. (2002). Constraints on the dynamics of mantle plumes from uplift of the Hawaiian Islands. *Earth and Planetary Science Letters*, *203*(1), 105–116. https://doi.org/10.1016/S0012-821X(02)00845-2